

# The carbon cycle of southeast Australia during 2019-2020: Drought, fires and subsequent recovery

This manuscript is a preprint and has been submitted for publication as a Research Article submitted to AGU Advances. Please note that the manuscript has yet to be formally accepted for publication. Subsequent versions of this manuscript may have slightly different content. If accepted, the final version of this manuscript will be available via the 'Peer-reviewed Publication DOI' link on the right-hand side of this webpage. Please feel free to contact any of the authors; we welcome feedback.

B. Byrne<sup>1</sup>, J. Liu<sup>1,2</sup>, M. Lee<sup>1</sup>, Y. Yin<sup>2</sup>, K. W. Bowman<sup>1,3</sup>, K. Miyazaki<sup>1</sup>, A. J. Norton<sup>1</sup>, J. Joiner<sup>4</sup>, D. F. Pollard<sup>5</sup>, D. W. T. Griffith<sup>6</sup>, V. A. Velasco<sup>6\*</sup>, N. M. Deutscher<sup>6</sup>, N. B. Jones<sup>6</sup>, and C. Paton-Walsh<sup>6</sup>

<sup>1</sup>Jet Propulsion Laboratory, California Institute of Technology, Pasadena, CA, USA

<sup>2</sup>Division of Geological and Planetary Sciences, California Institute of Technology, Pasadena, CA, USA

<sup>3</sup>Joint Institute for Regional Earth System Science and Engineering, University of California, Los Angeles, USA

<sup>4</sup>Laboratory of Atmospheric Chemistry and Dynamics, NASA Goddard Space Flight Center, Greenbelt, MD, USA

<sup>5</sup>National Institute of Water and Atmospheric Research Ltd (NIWA), Lauder, New Zealand

<sup>6</sup>Centre for Atmospheric Chemistry, School of Earth, Atmospheric and Life Sciences, University of Wollongong, Wollongong, New South Wales, Australia

\*Now at Deutscher Wetterdienst, German Meteorological Service Meteorological Observatory, Hohenpeissenberg Albin-Schwaiger-Weg 10 82383, Germany

Corresponding author: Brendan Byrne, [brendan.k.byrne@jpl.nasa.gov](mailto:brendan.k.byrne@jpl.nasa.gov), @BKAByrne

# The carbon cycle of southeast Australia during 2019–2020: Drought, fires and subsequent recovery

B. Byrne<sup>1</sup>, J. Liu<sup>1,2</sup>, M. Lee<sup>1</sup>, Y. Yin<sup>2</sup>, K. W. Bowman<sup>1,3</sup>, K. Miyazaki<sup>1</sup>, A. J. Norton<sup>1</sup>, J. Joiner<sup>4</sup>, D. F. Pollard<sup>5</sup>, D. W. T. Griffith<sup>6</sup>, V. A. Velasco<sup>6,\*</sup>, N. M. Deutscher<sup>6</sup>, N. B. Jones<sup>6</sup>, and C. Paton-Walsh<sup>6</sup>

<sup>1</sup>Jet Propulsion Laboratory, California Institute of Technology, Pasadena, CA, USA

<sup>2</sup>Division of Geological and Planetary Sciences, California Institute of Technology, Pasadena, CA, USA

<sup>3</sup>Joint Institute for Regional Earth System Science and Engineering, University of California, Los Angeles,

USA

<sup>4</sup>Laboratory of Atmospheric Chemistry and Dynamics, NASA Goddard Space Flight Center, Greenbelt, MD, USA

<sup>5</sup>National Institute of Water and Atmospheric Research Ltd (NIWA), Lauder, New Zealand

<sup>6</sup>Centre for Atmospheric Chemistry, School of Earth, Atmospheric and Life Sciences, University of

Wollongong, Wollongong, New South Wales, Australia

\*Now at Deutscher Wetterdienst, German Meteorological Service Meteorological Observatory,

Hohenpeissenberg Albin-Schwaiger-Weg 10 82383, Germany

©2021. All rights reserved. California Institute of Technology, government sponsorship acknowledged.

## Key Points:

- 113–236 TgC of CO<sub>2</sub> was released through biomass burning, and 19–52 TgC of CO<sub>2</sub> through reduced ecosystem productivity.
- Transition to cool-wet conditions resulted in robust recovery for unburned ecosystems but not for burned forests.
- Space-based remote sensing of trace gases and MODIS reflectances provide strong constraints on carbon cycle anomalies produced by extreme events.

---

Corresponding author: Brendan Byrne, [brendan.k.byrne@jpl.nasa.gov](mailto:brendan.k.byrne@jpl.nasa.gov)

## Abstract

2019 was the hottest and driest year on record for southeast Australia leading to bushfires of unprecedented extent. Ecosystem carbon losses due to drought and fire are believed to have been substantial, but have not been well quantified. Here, we utilize space-based measurements of trace gases (TROPOspheric Monitoring Instrument  $X_{\text{CO}}$ , Orbiting Carbon Observatory 2  $X_{\text{CO}_2}$ ) and up-scaled GPP (FluxSat GPP) to quantify the carbon cycle anomalies resulting from drought and fire in southeast Australia during the 2019–2020 growing season. We find that biomass burning released 113–236 TgC of  $\text{CO}_2$  while drought and fire-induced anomalies in net ecosystem exchange reduced growing season carbon uptake by an additional 19–52 TgC of  $\text{CO}_2$ . These carbon losses were concentrated during the spring and early summer, when hot-dry conditions were most severe. A shift to cooler conditions with above average rainfall during February is found to result in a partial recovery and greening in unburned ecosystems, but not in fire-impacted areas. The net 2019–2020 carbon loss substantially exceeded interannual variations in net uptake over 2010–2019 estimated from top-down constraints ( $\sim 5\sigma$  anomaly), and exceeded Australia’s annual fossil fuel emissions ( $\sim 104 \text{ TgC year}^{-1}$ ). Top-down constraints show that the regional carbon budget is strongly regulated by climate variability, and suggest cool-wet conditions are required for a rapid recovery of carbon stocks. This has implications for the regional carbon budget as more frequent climate-change-driven heat and drought events may increase the frequency of fire events and the recovery time of ecosystems, threatening the carbon stocks of the region.

## Plain Language Summary

Extreme climate events can have a large impacts on the carbon cycle of ecosystems. Droughts suppress photosynthesis, reducing the amount of  $\text{CO}_2$  absorbed from the atmosphere, and fires release  $\text{CO}_2$  to the atmosphere through combustion. In this study, we use satellite observations to quantify the disruption to the carbon cycle due to drought and bushfires in southeast Australia during 2019–2020. The drought and bushfires resulted in a carbon loss from these ecosystems that is greater than Australia’s annual fossil fuel emissions, although the carbon is expected to be drawn back into these ecosystems as the forests recover. This study highlights our ability to track the carbon cycle from space.

## 1 Introduction

Extreme drought and heat events can result in single-year carbon losses equal to many years of carbon sequestration (Ciais et al., 2005; Bastos et al., 2014). Hot-dry conditions can directly suppress both gross primary productivity (GPP) and ecosystem respiration (TER), with greater suppression of GPP leading to carbon loss (Reichstein et al., 2007; Sippel et al., 2018). These conditions can also precondition secondary carbon cycle disturbances, such as fires (D. M. J. S. Bowman et al., 2009; Abram et al., 2020), which in turn lead to increased carbon loss. Impacted ecosystems often experience legacy effects that can impact the carbon cycling for years after the extreme events have passed (Frank et al., 2015; Lindenmayer et al., 2021; Batllori et al., 2020).

Southeast Australia (Fig. 1) has a highly variable climate (Harris & Lucas, 2019; King et al., 2020), and frequently experiences both drought and fire. In fact, this susceptibility to fire has been a key factor in the evolution of the regional flora and fauna, acting as a process of disturbance and also regeneration (D. M. J. S. Bowman, 2000; Burrows, 2002). However, the region is experiencing more frequent, extensive and severe fires (Pitman et al., 2007; Stephens et al., 2013). A trend that is expected to continue with climate change (Perkins-Kirkpatrick & Gibson, 2017; Abatzoglou et al., 2019; Dowdy et al., 2019; Di Virgilio et al., 2019). Despite the adaptations of Australian ecosystems to fire, these changing fire regimes have been shown to impact tree mortality (Bennett et

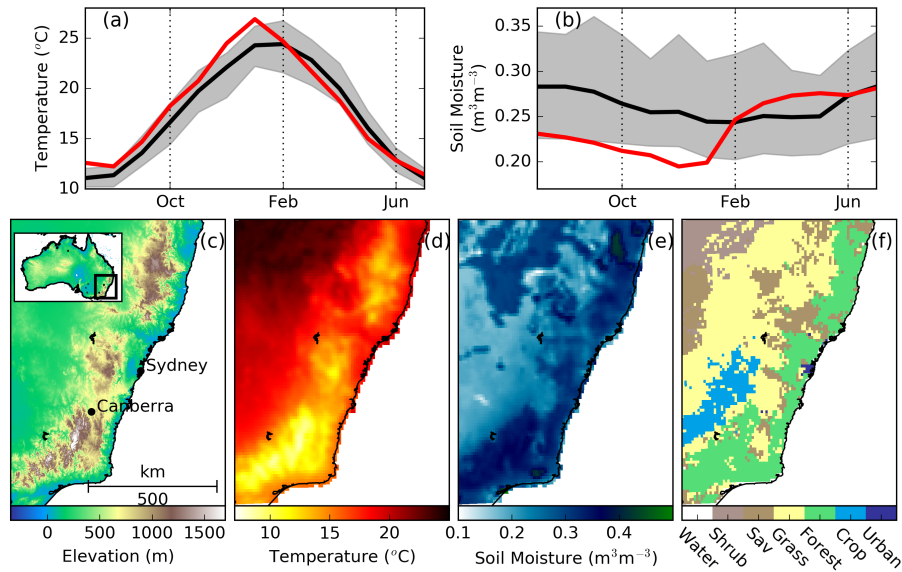


**Figure 1.** Climate and Geography of southeast Australia. (a) ERA5 Land soil temperature and (b) soil moisture over southeast Australia for 2010–2018 in black (shaded area showing the range) and 2019–2020 in red. (c) Surface elevation, (d) 2010–2018 mean soil temperature, (e) 2010–2018 mean soil moisture, and (f) MODIS IGBP vegetation type.

76 al., 2016; D. M. J. S. Bowman et al., 2014) and threaten the persistence of some forest  
 77 biomes in Australia (Fairman et al., 2016; D. M. J. S. Bowman et al., 2014; D. M. J. S. Bow-  
 78 man, Williamson, Price, et al., 2020), including their carbon stores. Thus, monitoring  
 79 the response of ecosystems in southeast Australia to extreme drought, heat and fire is  
 80 critical for understanding how the carbon balance of this region will evolve under climate  
 81 change.

82 Since 2017, southeast Australia has been in drought with the 2017–2019 period hav-  
 83 ing the largest three year rainfall deficit since 1900 (King et al., 2020). These conditions  
 84 have been most extreme during 2019, which was the hottest and driest year recorded in  
 85 southeast Australia (Abram et al., 2020; Bureau of Meteorology, 2020), precondition-  
 86 ing one of the worst bushfires seasons in recorded history (Nolan et al., 2020; King et  
 87 al., 2020; Deb et al., 2020; Boer et al., 2020; Ward et al., 2020; Collins, Bradstock, et al.,  
 88 2021; D. M. J. S. Bowman et al., 2021). These extreme conditions subsided in early Febru-  
 89 ary 2020 with heavy rainfall and cooler conditions that persisted throughout the aus-  
 90 tral autumn. This combination of drought and fire, followed by heavy rainfall imparts  
 91 a large and complex perturbation on the carbon cycle of the region and impacted forested  
 92 regions that cover much of the southeast coast and mountainous regions, and more arid  
 93 savanna, grassland and cropland ecosystems further inland (Fig. 1).

94 The impact of extreme drought and heat events on ecosystems are complex and  
 95 challenging to monitor. Ecosystem responses are sensitive to the specific characteristics  
 96 of the event, such as the intensity and timing (Bastos et al., 2014; Frank et al., 2015; De Boeck  
 97 et al., 2011; Denton et al., 2017), legacy effects from previous disturbances (Longo et al.,  
 98 2020; Bowd et al., 2021) and vegetation type (Zhang et al., 2016; Turner et al., 2020).  
 99 The recent expansions of space-based observing systems of carbon-cycle-relevant quan-  
 100 tities are now providing the opportunity for finer scale quantification of carbon cycle per-

101 turbations and more detailed understanding of the response of ecosystems to extreme  
 102 drought, heat and fire (Byrne et al., 2019; Byrne, Liu, Lee, et al., 2020; Byrne, Liu, Bloom,  
 103 et al., 2020; Yin, Bloom, et al., 2020; Turner et al., 2020). In this study, we utilize space-  
 104 based observations to provide a comprehensive analysis of the carbon cycle perturbations  
 105 due to extreme drought, heat and fire during the 2019–2020 growing season in southeast  
 106 Australia.

107 We combine observations from multiple satellites to quantify the carbon cycle anoma-  
 108 lies within southeast Australia. We employ TROPospheric Monitoring Instrument (TROPOMI)  
 109 CO column abundance measurements (Landgraf et al., 2016; Borsdorff et al., 2018) to  
 110 quantify biomass burning emissions. Anomalies in net ecosystem exchange (NEE, which  
 111 is defined as the residual between ecosystem respiration and GPP) are obtained by com-  
 112 bining top-down constraints on net surface-atmosphere CO<sub>2</sub> fluxes from column-averaged  
 113 dry-air mole fractions of CO<sub>2</sub> ( $X_{\text{CO}_2}$ ) measurements from the Orbiting Carbon Obser-  
 114 vatory 2 (OCO-2) (Crisp et al., 2017; Eldering et al., 2017) with estimates of GPP anoma-  
 115 lies from FluxSat (Joiner & Yoshida, 2020), which produces GPP from MODIS reflectances  
 116 trained against FLUXNET sites.

117 The combination of these newly available observations offers a unique opportunity  
 118 to monitor individual components of the carbon cycle anomalies across southeast Aus-  
 119 tralia during 2019–2020. Specifically, we aim to answer: How much CO<sub>2</sub> was released  
 120 to the atmosphere due to drought and biomass burning, respectively? How did this event  
 121 impact forest and non-forest ecosystems differently? What were the differences in car-  
 122 bon cycle perturbations between burned and unburned ecosystems? And how does 2019–  
 123 2020 compare with previous years? To that end, we first quantify biomass burning emis-  
 124 sions of CO from the TROPOMI observations, which are then converted to CO<sub>2</sub> emis-  
 125 sions (Sec. 3.1). Then, an anomaly in atmospheric CO<sub>2</sub> ( $\Delta\text{CO}_2$ ) is derived from the OCO-  
 126 2 measurements (Sec. 3.2). This top-down constraint is then combined with estimates  
 127 of GPP anomalies from FluxSat to derive NEE anomalies over the 2019–2020 growing  
 128 season (Sec. 3.3). We then synthesize these estimates and present the evolution of car-  
 129 bon cycle anomalies over the 2019–2020 growing season (Sec. 4), and compare this event  
 130 with the regional carbon budget over the 2010–2019 period (Sec. 5). This is followed by  
 131 a discussion of our biomass burning emission estimates in the context of previous bot-  
 132 tom up estimates (Sec. 6.1), the implications of this extreme event for the carbon cy-  
 133 cle of southeast Australia (Sec. 6.2), and the uncertainties and remaining challenges in  
 134 estimating carbon fluxes from extreme events (Sec 6.3). Finally, we provide our conclu-  
 135 sions in Sec. 7.

## 136 2 Environmental and Geographical data

137 Environmental and geographical data are used to help interpret the carbon cycle  
 138 anomalies. We examine the covariations of carbon cycle anomalies with variations in soil  
 139 temperature and soil moisture from ERA5-Land reanalysis (Munoz Sabater, 2019), gen-  
 140 erated using Copernicus Climate Change Service Information 2020. For this analysis,  
 141 we calculate the area-weighted soil moisture and temperature over the top 1 m of soil.  
 142 Vegetation land cover is obtained from the MODIS land cover dataset (MCD12C1) (Friedl  
 143 & Sulla-Menashe, 2015) and elevation data are obtained from ETOPO1 (Amante & Eakins,  
 144 2009).

## 145 3 CO<sub>2</sub> Flux Estimates

146 Figure 2 shows a schematic diagram of the methods used to estimate biomass burn-  
 147 ing and anomalies in NEE ( $\Delta\text{NEE}$ ). Biomass burning CO<sub>2</sub> emissions are estimated from  
 148 TROPOMI  $X_{\text{CO}}$  measurements (Sec. 3.1). First, emissions of CO are estimated through  
 149 flux inversion analyses that assimilate TROPOMI  $X_{\text{CO}}$  measurements. Then CO emis-  
 150 sions are converted to CO<sub>2</sub> emissions using emission factors.

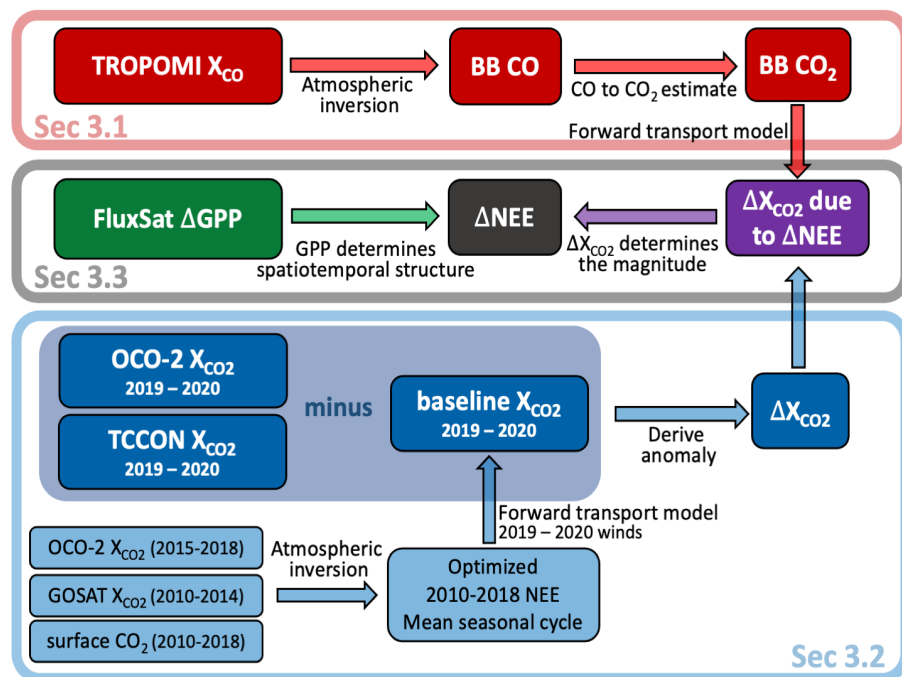


**Figure 2.** Schematic diagram of the method used to derive biomass burning and  $\Delta\text{NEE}$   $\text{CO}_2$  fluxes. Biomass burning emissions are based on TROPOMI  $X_{\text{CO}}$  measurements (shown in red).  $\text{CO}_2$ -based estimates of  $\Delta X_{\text{CO}_2}$  are estimated from measurements of atmospheric  $\text{CO}_2$  (shown in blue). First, NEE fluxes over 2010–2018 are estimated through flux inversion analysis (shown in light blue). Combining the mean NEE seasonal cycle over this period with a chemical transport model, we simulate the expected 2019–2020 baseline atmospheric  $\text{CO}_2$  fields given climatological fluxes. Then, the difference between the actual 2019–2020 measurements and the expected  $X_{\text{CO}_2}$  gives the anomaly in atmospheric  $X_{\text{CO}_2}$  (shown in blue shaded area).  $\Delta\text{NEE}$  is then estimated from combining all of the constraints. The spatiotemporal structure of  $\Delta\text{NEE}$  is based on FluxSat GPP (shown in green), while the magnitude is derived from combining the top-down and biomass-burning-derived  $\Delta\text{CO}_2$  estimates (shown in purple).

151 Estimates of  $\Delta\text{NEE}$  are obtained through combining several different data sources.  
 152 First, we infer a top-down  $\text{CO}_2$  anomaly signal ( $\Delta X_{\text{CO}_2}$ ) due to anomalies in biosphere-  
 153 atmosphere  $\text{CO}_2$  fluxes (Sec. 3.2). Then we subtract the  $\Delta X_{\text{CO}_2}$  signal due to biomass  
 154 burning emissions, giving  $\Delta X_{\text{CO}_2}$  due to  $\Delta\text{NEE}$ . This provides a constraint on the mag-  
 155 nitude of  $\Delta\text{NEE}$ . Finally, we estimate spatiotemporal structure of  $\Delta\text{NEE}$  by combining  
 156 the atmospheric  $\text{CO}_2$  constraints with FluxSat GPP (Sec. 3.3). Note that the  $\text{CO}_2$  flux  
 157 and atmospheric  $X_{\text{CO}_2}$  are related to fluxes using a chemical transport model (Sec. 3.1.1).

158 Atmospheric chemical transport simulations and flux inversions are performed with  
 159 the Greenhouse Gas Framework - Flux (GHGF-Flux) inversion system. GHGF-Flux is  
 160 a flux inversion system developed under the NASA Carbon Monitoring System Flux (CMS-  
 161 Flux) project (<https://cmsflux.jpl.nasa.gov>), and inherits the chemistry transport model  
 162 from the GEOS-Chem and the adjoint model from the GEOS-Chem adjoint (Henze et  
 163 al., 2007; Liu et al., 2014). Chemical transport is driven by the Modern Era Retrospec-  
 164 tive Analysis for Research and Applications, Version 2 (MERRA-2) meteorology produced  
 165 with version 5.12.4 of the Goddard Earth Observing System (GEOS) atmospheric data  
 166 assimilation system (Gelaro et al., 2017). To perform tracer transport, these fields are  
 167 regridded to the desired horizontal resolution and archived with a temporal resolution  
 168 of three hours except for surface quantities and mixing depths, which have a temporal  
 169 resolution of one hour. Flux inversions are performed using 4-D variational assimilation  
 170 (4D-Var), with the details provided in the subsections.

### 171 3.1 Biomass burning emissions

172 Atmospheric CO inversions have been shown to be an effective top-down approach  
 173 for estimating fire carbon emissions (Yin et al., 2015, 2016; Yin, Bloom, et al., 2020; Liu  
 174 et al., 2017; Zheng et al., 2019; Langenfelds et al., 2002). Here, we perform atmospheric  
 175 CO inversions to estimate biomass burning emissions by assimilating TROPOMI retrievals  
 176 of ( $X_{\text{CO}}$ ). TROPOMI is a grating spectrometer aboard ESA’s Sentinel-5 Precursor (S-  
 177 5P) satellite that measures Earth reflected radiances (Veeffkind et al., 2012). CO total  
 178 column densities are retrieved in the shortwave infrared (around  $2.3 \mu\text{m}$ ) using the Short-  
 179 wave Infrared CO Retrieval (SICOR) algorithm (Landgraf et al., 2016). Retrieved CO  
 180 total column densities are then converted to dry-air mole fractions of CO ( $X_{\text{CO}}$ ) using  
 181 the dry-air surface pressure and hypsometric equation. The column averaging kernel is  
 182 similarly converted to mole-fraction space.

183 Biomass burning CO emissions are estimated using one-way nested flux inversions  
 184 over Australia ( $100^\circ - 177.5^\circ \text{ E}$ ,  $0^\circ - 60^\circ \text{ S}$ ) at  $0.5^\circ \times 0.625^\circ$  spatial resolution. Nested  
 185 flux inversions are performed from 5 Nov 2019 through 14 Jan 2020 (to cover the period  
 186 with the majority of fires) and assimilate TROPOMI  $X_{\text{CO}}$  super-obs (aggregated obser-  
 187 vations) to optimize scaling factors for each gridcell over the entire period. Details on  
 188 the inversion configuration are provided in Appendix A. The posterior scale factors are  
 189 then applied over the entire Oct–May time period (note that biomass burning emissions  
 190 are small outside of the inversion period).

191 Eight nested flux inversions are performed, which vary in prior biomass burning  
 192 emissions, quantities optimized, and boundary conditions (Table 1). Differences in flux  
 193 inversion configuration are employed to test the sensitivity of posterior fluxes to the in-  
 194 version set-up. We employ two different biomass burning emissions datasets as prior CO  
 195 fluxes, namely the Global Fire Emissions Database version 4 (GFED4.1s) (van der Werf  
 196 et al., 2017) and Global Fire Assimilation System (GFAS) (Kaiser et al., 2012). GFED4.1s  
 197 provides estimates of biomass burning using MODIS 500 m burned area (Giglio et al.,  
 198 2013), 1 km thermal anomalies, and 500 m surface reflectance observations to statisti-  
 199 cally estimate burned area associated with small fires (Randerson et al., 2012). GFAS  
 200 v1.2 provides estimates of daily biomass burning emissions by assimilating MODIS fire  
 201 radiative power observations (Di Giuseppe et al., 2018; Kaiser et al., 2012). For both datasets,

**Table 1.** Flux inversion set-up for the eight nested TROPOMI CO flux inversions.

Inversion	prior BB emissions	Boundary conditions	Optimized fluxes
1	GFED4.1s	optimized	mean BB diurnal BB
2	GFED4.1s	optimized	mean BB
3	GFED4.1s	opt + 10 ppb	mean BB diurnal BB
4	GFED4.1s	opt + 10 ppb	mean BB
5	GFASv1.2	optimized	mean BB diurnal BB
6	GFASv1.2	optimized	mean BB
7	GFASv1.2	opt + 10 ppb	mean BB diurnal BB
8	GFASv1.2	opt + 10 ppb	mean BB

202 we incorporate the impact of the diurnal cycle based on Mu et al. (2011). The inversions  
 203 also differ by either prescribing or optimizing diurnal variations on biomass burning emis-  
 204 sions. Finally, inversions are either run using boundary conditions from a global TROPOMI  
 205 flux inversion or with these boundary conditions adjusted by adding 10 ppb (roughly equiv-  
 206 alent to the mean data-model difference) at all levels and times to test the sensitivity  
 207 of the nested CO inversion to lateral boundary conditions.

208 Video 1 [Figure 3/supp Video 1 in pre-print] shows the spatial distribution of the  
 209 mean posterior fluxes and  $X_{CO}$  measurements across southeast Australia. Biomass burn-  
 210 ing emissions were most concentrated in forest ecosystems along the coast and further  
 211 inland along the border between New South Wales and Victoria. Posterior CO emissions  
 212 are increased for all inversion configurations, with a posterior mean CO emission esti-  
 213 mate of 15.6 TgC (range: 9.7–24.3 TgC), relative to prior emission estimates of 11.4 TgC  
 214 for GFED and 5.8 TgC for GFAS over the growing season. The largest source of spread  
 215 among posterior fluxes is due to the prior biomass burning flux employed, with GFED-  
 216 based inversions giving larger posterior emissions than GFAS-based inversions (see Fig-  
 217 ure S2 in the supporting information).

218 The performance of the nested CO flux inversions are evaluated by comparing the  
 219 posterior CO fields with the TROPOMI  $X_{CO}$  measurements, independent  $X_{CO}$  measure-  
 220 ments from the nearby Wollongong (Griffith et al., 2014) and Lauder (Pollard et al., 2019,  
 221 2017) Total Column Carbon Observing Network (TCCON) (Wunch et al., 2011) sites,  
 222 the Cross-track Infrared Sounder (CrIS) and surface-based flask and in situ measurements  
 223 at the nearby Cape Grim (CGO), Baring Head (BHD), and Lauder (LAU) sites. CrIS  
 224 is a Fourier Transform Spectrometer aboard the satellite Suomi-NPP satellite and has  
 225 a spectral resolution of  $0.625 \text{ cm}^{-1}$  and a ground pixel diameter of 14 km at nadir. CrIS  
 226 and TROPOMI make collocated measurements because Suomi-NPP and Sentinel 5p are  
 227 in a tandem orbit with a roughly 10 min separation. However, CrIS takes measurements  
 228 in both day and night. The retrieval of CO uses the MUlti-SpEctra, MUlti-SpEcies, MUlti-  
 229 SENSors (MUSES) algorithm (Fu et al., 2016) that is based on the optimal estimation  
 230 method with heritage from the Tropospheric Emission Spectrometer (TES) (K. W. Bow-  
 231 man et al., 2006). We generate  $X_{CO}$  measurements from version 1.8 of the L2 tropospheric



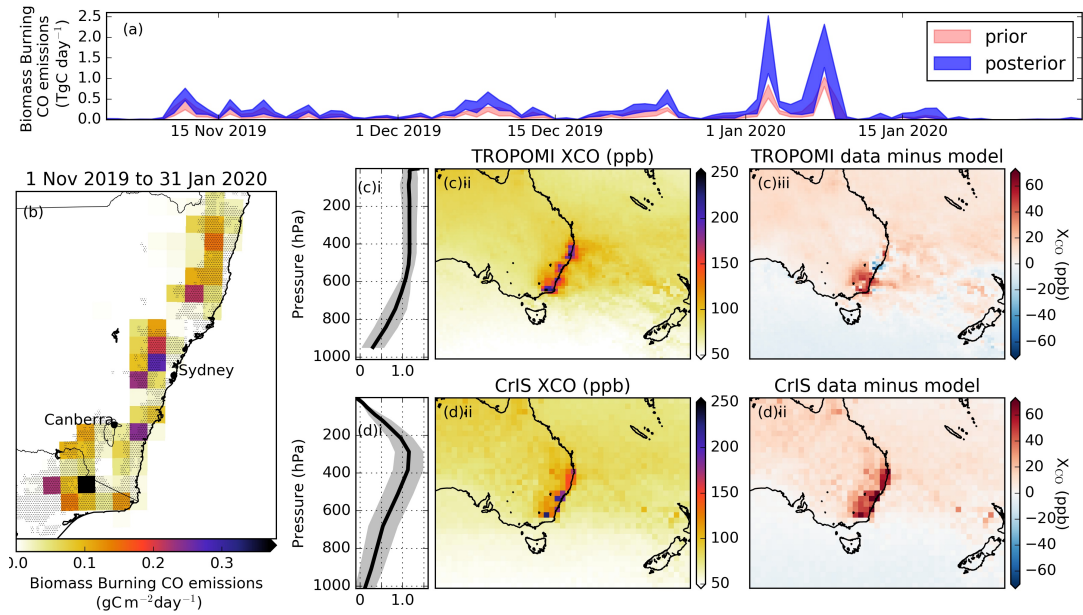


**Figure 3.** [See Video 1] (a) Timeseries showing the range of prior (red) and posterior (blue) biomass burning CO emissions over southeast Australia. (b) Mean posterior biomass burning emissions at  $0.5^\circ \times 0.625^\circ$  spatial resolution. Hatching indicates the locations of forested areas. (c) TROPOMI (i) mean  $X_{CO}$  column averaging kernel, (ii) mean  $X_{CO}$  and (iii) posterior data-model mismatch at  $0.5^\circ \times 0.625^\circ$  spatial resolution. (d) CrIS (i) mean  $X_{CO}$  column averaging kernel, (ii) mean  $X_{CO}$  and (iii) posterior data-model mismatch at  $1.0^\circ \times 1.0^\circ$  spatial resolution.

232 CO profile product, and compare posterior CO fields against daytime and nighttime  $X_{\text{CO}}$   
 233 measurements separately.

234 As trace gas emissions from fires are impacted by pyroconvective motions (that are  
 235 not well represented in chemical transport models), we evaluate the posterior fluxes with  
 236 two sets of model runs that release the CO emissions at different model levels. In one  
 237 set of runs, we release the emissions at the surface (as was done in the inversion), while  
 238 in the second set we release CO emissions at the injection height (mean altitude of max-  
 239 imum injection) simulated by a plume rise model (IS4FIRES) (Rémy et al., 2017), which  
 240 was provided with the GFAS emission data. Here we provide a brief summary of the eval-  
 241 uation, while a detailed evaluation of the flux inversions is presented in Text S1 of the  
 242 supporting information. Posterior fluxes generally show better agreement with the TROPOMI,  
 243 TCCON, CrIS, and the in situ/flask measurements. This is true for all measurements  
 244 and a subset of measurements that are biomass-burning-sensitive. However, posterior  
 245 CO fluxes tend to underestimate  $X_{\text{CO}}$  for biomass-burning-sensitive measurements (but  
 246 less so than the prior). This residual mismatch is likely related to transport model er-  
 247 rors, as the modeled observations often show differences in plume structure (Video 1/Fig. 3).  
 248 Furthermore, the transport model underestimates vertical motions around the bushfires,  
 249 which were impacted by pyroconvection. The impact of weak modeled vertical motions  
 250 can be seen in Video 1c,d/Figure 3c,d. The column averaging kernel for TROPOMI shows  
 251 greater sensitivity to CO between 400 hPa and the surface, while CrIS shows greater sen-  
 252 sitivity to CO in the upper troposphere. Both TROPOMI and CrIS show mean  $X_{\text{CO}}$  mole  
 253 fractions greater than 200 ppb in southeast Australia for the duration of the biomass burn-  
 254 ing over Nov–Jan. However, posterior data-model mismatches are much less positive for  
 255 TROPOMI than for CrIS, implying that vertical motions are underestimated and the  
 256 CO emissions do not reach the upper troposphere to the levels observed.

257 Finally, to estimate CO<sub>2</sub> biomass burning emissions we apply the ratio of CO<sub>2</sub> to  
 258 CO emission factors (that are constant in time). We apply the emission factors from the  
 259 biomass burning database used as the prior (e.g., either GFAS or GFED). The emission  
 260 ratios are variable by vegetation type, but aggregating for fires across Australia gives ef-  
 261 fective CO<sub>2</sub>/CO emission ratios of 12.01 for GFED and 11.30 for GFAS. Differences are  
 262 primarily driven by differences in emission factors for forest emissions, but are within  
 263 the natural variation of emission factors reported by Akagi et al. (2011) (see Text S2 and  
 264 Fig. S4 in the supporting information) and reported for Australian forests (Table S5) (Paton-  
 265 Walsh et al., 2014; Guérette et al., 2018). The impact of emission factor uncertainty is  
 266 further discussed in Sec. 6.3.2.

### 267 **3.1.1 Atmospheric $\Delta\text{CO}_2$ signal simulation**

268 We simulate the biomass burning  $X_{\text{CO}_2}$  anomaly signal ( $\Delta X_{\text{CO}_2 \text{ BB}}$ ) by running  
 269 the nested chemical transport model. The  $\Delta X_{\text{CO}_2 \text{ BB}}$  signal is calculated by perform-  
 270 ing simulations with climatological fluxes and with the climatological fluxes plus the biomass  
 271 burning estimates, then taking the difference between these two simulations at the OCO-  
 272 2 and TCCON measurements locations to isolate the signal due to biomass burning. We  
 273 simulate OCO-2 good-quality land (land glint and land nadir) and ocean glint super-obs  
 274 (aggregated to  $0.5^\circ \times 0.5^\circ$  resolution grids following Liu et al. (2017), with the additional  
 275 requirement that there must be a minimum of three OCO-2 observations within each  $0.5^\circ \times 0.5^\circ$   
 276 grid box per track). For TCCON measurements, we use all good quality data.

### 277 **3.2 Top-down $\Delta\text{CO}_2$ signal**

278 The top-down estimate of  $\Delta X_{\text{CO}_2}$  ( $\Delta X_{\text{CO}_2 \text{ top-down}}$ ) is calculated based on the data-  
 279 model difference between OCO-2 and TCCON measurements and simulated CO<sub>2</sub> fields  
 280 based on climatological NEE emissions.

281 Climatological NEE fluxes are generated through CO<sub>2</sub> flux inversion analyses. We  
 282 generate climatological NEE fluxes as the average over the period 2010–2018. Fluxes over  
 283 2010–2014 are taken as the mean GOSAT+surface+TCCON inversion of Byrne, Liu, Lee,  
 284 et al. (2020). To generate climatological fluxes over 2015–2019, we perform a flux inver-  
 285 sion at 4°×5° assimilating OCO-2 measurements and surface-based CO<sub>2</sub> measurements  
 286 concurrently and use the identical inversion set-up to Byrne, Liu, Lee, et al. (2020). For  
 287 surface measurements, we use version 6.0 of the GLOBALVIEW plus package (Masarie  
 288 et al., 2014; Cooperative Global Atmospheric Data Integration Project, 2018). For OCO-  
 289 2 measurements, we use ACOS b10 land (land glint and land nadir) and ocean glint re-  
 290 trievals aggregated into super-obs at 0.5°×0.5° resolution grids following Liu et al. (2017),  
 291 with the additional requirement that there must be a minimum of three OCO-2 obser-  
 292 vations within each 0.5°×0.5° grid box per track. We use all data that pass the qual-  
 293 ity flag filter. This 2015–2019 flux inversion is referred to as the “IS+LNLGOG” inver-  
 294 sion.

295 Calculations of the  $\Delta X_{\text{CO}_2 \text{ top-down}}$  signal are performed with the one-way nested  
 296 grid over Australia. First, we generate boundary conditions by performing a simulation  
 297 at 2°×2.5° with regrided optimized NEE and ocean fluxes and prescribed fluxes from  
 298 the 4°×5° flux inversion. Then we run the nested model and sample the OCO-2 and TC-  
 299 CON observations from 1 Oct 2019 through 31 Jan 2020. Finally, we calculate the  $\Delta X_{\text{CO}_2 \text{ top-down}}$   
 300 anomaly signal as the data-model mismatch for these simulated observations.

### 301 3.3 NEE anomaly estimate

302 NEE anomalies ( $\Delta \text{NEE}$ ) over the 2019–2020 growing season are estimated by combin-  
 303 ing the constraints on GPP from FluxSat Version 2 (Joiner & Yoshida, 2020) with  
 304 the constraints on the net CO<sub>2</sub> flux from the top-down  $\Delta X_{\text{CO}_2 \text{ top-down}}$  signal and biomass-  
 305 burning- $\Delta X_{\text{CO}_2 \text{ BB}}$ . The spatial and temporal structure of  $\Delta \text{NEE}$  is assumed to be di-  
 306 rectly proportional to  $\Delta \text{GPP}$  from FluxSat, while the magnitude of the  $\Delta \text{NEE}$  is inferred  
 307 from the atmospheric  $\Delta X_{\text{CO}_2}$  signal.

308 FluxSat estimates GPP based on Nadir BRDF-Adjusted Reflectances (NBAR) from  
 309 the MODerate-resolution Imaging Spectroradiometer (MODIS) MYD43D product (Schaaf  
 310 et al., 2002). The GPP estimates are calibrated with the FLUXNET 2015 GPP derived  
 311 from eddy covariance flux measurements at Tier 1 sites (Joiner & Yoshida, 2020). The  
 312 native spatiotemporal resolution of FluxSat GPP is daily on a 0.05°×0.05° grid. For  
 313 our analysis, we regrid spatially to 0.1°×0.1° while retaining daily temporal resolution.  
 314 We calculate  $\Delta \text{GPP}$  from FluxSat as the difference between fluxes for 2019–2020 rela-  
 315 tive to a 2010–2018 mean.

316 NEE is defined as  $\text{NEE} = R_{\text{hetero}} - \text{NPP}$ , where NPP is net primary production  
 317 and  $R_{\text{hetero}}$  is heterotrophic respiration. Therefore,  $\Delta \text{NEE}$  is due to both anomalies in  
 318 NPP, where  $\text{NPP} \approx 0.5 \times \text{GPP}$  (Waring et al., 1998; DeLucia et al., 2007; Collalti & Pren-  
 319 tice, 2019), and  $R_{\text{hetero}}$ . For this analysis we also assume  $\Delta \text{NEE} \propto -\Delta \text{GPP}$ , as there are  
 320 no direct large scale observations that can be related to  $R_{\text{hetero}}$ . Empirical evidence from  
 321 the OzFlux eddy covariance network (Li et al., 2017) has found that  $\Delta \text{NEE}$  can be ex-  
 322 pressed linearly as a function of  $\Delta \text{GPP}$  with reasonable accuracy. Li et al. (2017) find  
 323 that  $\Delta \text{NEE} = -0.24 \Delta \text{GPP}$  for non-forest ecosystems, where anomalies in GPP and res-  
 324 piration are correlated, but  $\Delta \text{NEE} = -0.8 \Delta \text{GPP}$  for forest ecosystems, where GPP and  
 325 respiration do not co-vary.

326 To estimate the magnitude of  $\Delta \text{NEE}$ , we simulate the OCO-2 observed  $X_{\text{CO}_2}$  anomaly  
 327 signal due to  $\Delta \text{GPP}$  ( $\Delta X_{\text{CO}_2 \text{ GPP}}$ ) using the same approach as was used for biomass burn-  
 328 ing (See 3.1.1). We invert a magnitude of  $\Delta \text{NEE}$  through regressions of  $\Delta X_{\text{CO}_2 \text{ NEE}}$  against  
 329 an observationally constrained anomaly in  $X_{\text{CO}_2}$ :

$$\Delta X_{\text{CO}_2 \text{ NEE}} + \beta = -\alpha \times \Delta X_{\text{CO}_2 \text{ GPP}} + \beta = \Delta X_{\text{CO}_2 \text{ top-down}} - \Delta X_{\text{CO}_2 \text{ BB}}. \quad (1)$$

**Table 2.** Coefficients ‘ $\alpha$ ’ obtained by linear regressions that relates  $\Delta\text{NEE}$  and  $\Delta\text{GPP}$  through the relationship  $\Delta\text{NEE} = -\alpha\Delta\text{GPP}$ . The median and range of  $\alpha$  are given for regressions using the eight posterior biomass burning estimates for simulations that vary in the emission height and forest/non-forest parameterization. The bottom row gives the mean and range for the truncated distribution of all simulations, wherein we remove largest and smallest two outliers from the 32 simulations performed by varying biomass burning emissions, emission height, and the forest/non-forest parameterization.

emission height	forest/non-forest parameterization	forest $\alpha$	non-forest $\alpha$
		median (range)	median (range)
injection height	0.24N + 0.8F	0.52 (0.33–1.15)	0.16 (0.10–0.35)
injection height	N + F	0.26 (0.21–0.42)	0.26 (0.21–0.42)
surface	0.24N + 0.8F	0.59 (0.42–0.66)	0.18 (0.12–0.20)
surface	N + F	0.31 (0.23–0.32)	0.31 (0.23–0.32)
		mean (range)	mean (range)
all (truncated)	all (truncated)	0.41 (0.23–0.66)	0.23 (0.13–0.35)

330 Note that  $\beta$  is included to account for possible small residual biases from the observa-  
 331 tions or model. Initially, we attempted a multivariate regression to solve this for forest  
 332 and non-forest  $\Delta X_{\text{CO}_2 \text{ NEE}}$  individually but recovered unrealistic negative coefficients  
 333 for forests. The  $\Delta X_{\text{CO}_2 \text{ NEE}}$  for forests is relatively small and may be impacted by er-  
 334 rors in biomass burning emissions and transport, potentially limiting our ability to dif-  
 335 ferentiate forest and non-forest  $\Delta\text{NEE}$ . To avoid these unphysical values, we prescribe  
 336 the the ratio of  $\Delta\text{NEE}$  between forest and non-forest ecosystems. Following from Li et  
 337 al. (2017), we perform one set of regressions using

$$\Delta\text{NEE}_{\text{total}} = -\alpha [0.24 \Delta\text{GPP}_{\text{non-forest}} + 0.8 \Delta\text{GPP}_{\text{forest}}]. \quad (2)$$

338 However, due to the large  $\text{CO}_2$  biomass burning emissions over this event, it is possible  
 339 that  $\Delta\text{NEE}$  and  $\Delta\text{GPP}$  may diverge from this relationship. Therefore, we also perform  
 340 a second set of regressions using the relationship:

$$\Delta\text{NEE}_{\text{total}} = -\alpha [\Delta\text{GPP}_{\text{non-forest}} + \Delta\text{GPP}_{\text{forest}}]. \quad (3)$$

341 We perform a series of linear regressions using Eq. 1 to estimate ‘ $\alpha$ ’, the param-  
 342 eter that relates  $\Delta\text{NEE}$  and  $\Delta\text{GPP}$ . This regression is performed a total of 32 times by  
 343 varying the emission height of biomass burning emissions between the surface and in-  
 344 jection height, the posterior biomass burning emissions estimated by the eight TROPOMI  
 345 flux inversions, and the parameterization relating forest and non-forest  $\Delta\text{NEE}$  using Eqs 2–  
 346 3. Table 2 shows the statistics of  $\alpha$  for these 32 regressions. The best estimate of  $\alpha$  is  
 347 then calculated as the mean of the truncated distribution of the 32  $\alpha$  values, with the  
 348 largest and smallest two values removed, and the range of the truncated distribution is  
 349 taken as the uncertainty. This gives an  $\alpha$  of 0.41 (0.23–0.66) for forest ecosystems, which  
 350 is half the value of Li et al. (2017), and 0.23 (0.13–0.35) for non-forest ecosystem, which  
 351 is almost identical to the value of Li et al. (2017). These  $\alpha$  values are applied to estimate  
 352  $\Delta\text{NEE}$  over the entire growing season.

353 A comparison of  $\Delta X_{\text{CO}_2 \text{ top-down}}$  and the simulated  $\Delta X_{\text{CO}_2 \text{ GPP}} + \Delta X_{\text{CO}_2 \text{ BB}}$  sig-  
 354 nal for TCCON and OCO-2 measurements is shown in the supporting information (Fig. S6).  
 355 The flux estimates found here are generally consistent with these top-down datasets, al-

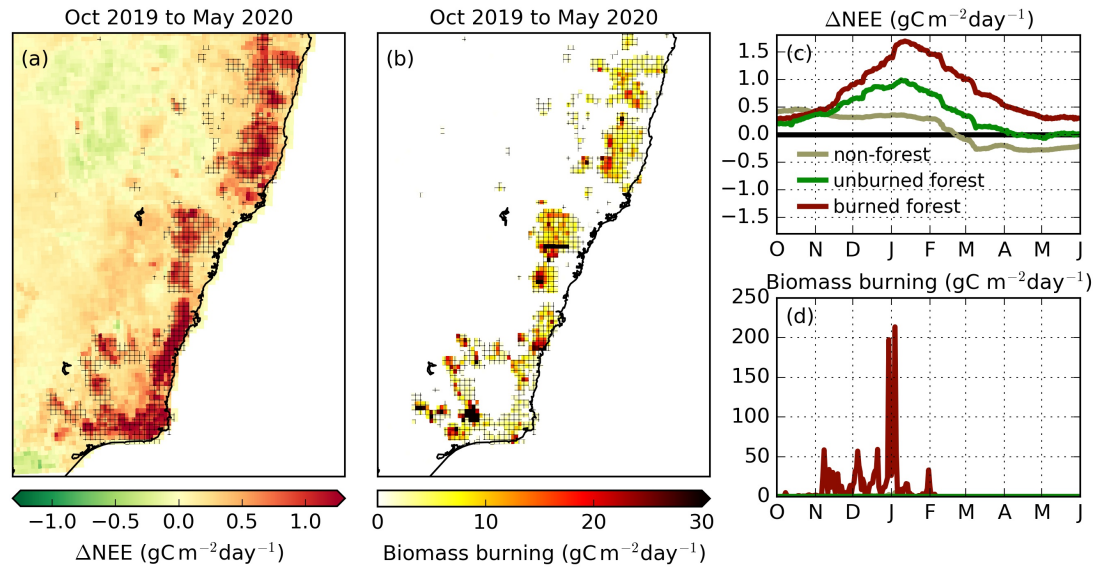


**Figure 4.** [See Video 2] Daily (a)  $\Delta$ NEE and (b) biomass burning emissions over southeast Australia. Hatching shows burned area. Timeseries of (c)  $\Delta$ NEE and (b) biomass burning for light grey) non-forest, (green) unburned forest and (red) burned forest areas.

356 though there is considerable scatter between different TCCON sites and OCO-2 view-  
 357 ing modes. Data–model mismatches for individual retrievals are strongly impacted by  
 358 retrieval errors and model errors in simulating the observations, however, aggregating  
 359 to 0.2 ppm intervals in the flux signal reveals strong positive correlations ( $R^2 > 0.9$ ,  
 360 Fig. S6). Similarly, simulated boundary layer  $\text{CO}_2$  at Cape Grim and Lauder show im-  
 361 proved agreement with the measurements when the flux anomalies are included, while  
 362 results at Baring Head are mixed (Table S6).

#### 363 4 Carbon cycle anomalies over the 2019–2020 growing season

364 The climate anomalies over the 2019–2020 growing season can be partitioned into  
 365 two phases. Warm–dry conditions dominated the region during the austral spring and  
 366 early summer (October through January), when there were a number of biomass burn-  
 367 ing events, primarily in the forested regions. This was followed by a cooler–wetter pe-  
 368 riod during February through May (Fig. 1a,b). Video 2 [Figure 4/supp Video 2 in pre-  
 369 print] shows the evolution of  $\Delta$ NEE and biomass burning over the 2019–2020 growing  
 370 season. During the warm–dry phase, GPP was suppressed across the region, falling be-  
 371 low the range of observed GPP over the 2010–2018 period ( $2.0 \text{ gC m}^{-2} \text{ day}^{-1}$  for Oct-  
 372 Jan 2019–2020 versus  $3.0\text{--}4.3 \text{ gC m}^{-2} \text{ day}^{-1}$  over 2010–2018). Suppression of productiv-  
 373 ity occurred uniformly across southeast Australia during Oct–Jan (Fig. 5), impacting both  
 374 forest and non-forest ecosystems. This is followed by a large-scale recovery in GPP to  
 375 above average values during Feb–May, when cooler–wetter conditions dominate. This re-  
 376 covery was relatively uniform across the region with the exception of burned areas (in-  
 377 dicated by hatching in Fig. 5), which show suppression of GPP during Feb–May that is  
 378 similar to Oct–Jan.

379 Figure 6 shows the timeseries of  $\Delta$ GPP for forest and combined non-forest ecosys-  
 380 tems (includes cropland, grassland, shrubland, and savanna ecosystems) over southeast

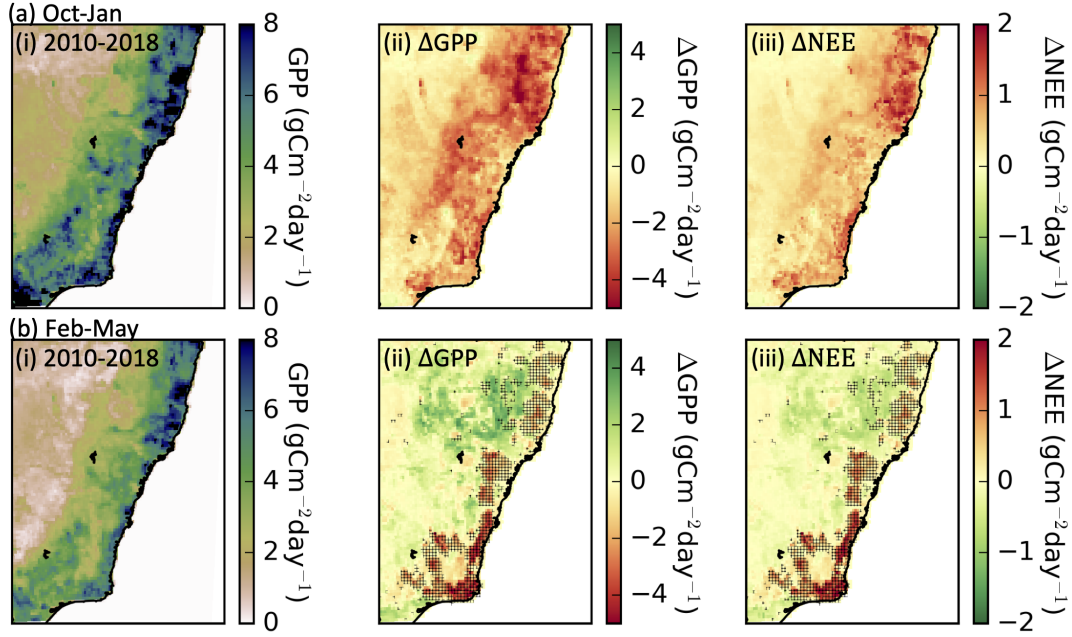


**Figure 5.** (a) Oct-Jan and (b) Feb-May maps of (i) 2010-2018 mean GPP, (ii)  $\Delta$ GPP (2019-2020 GPP minus 2010-2018 mean GPP) and (iii) mean estimate of  $\Delta$ NEE. Hatching shows locations of bushfires during the 2019-2020 growing season.

**Table 3.** Oct–May net CO<sub>2</sub> fluxes (TgC) due to biomass burning and  $\Delta$ NEE over southeast Australia.

	non-forest	burned forest	unburned forest	All
BB	20 (18–23)	146 (95–213)	0	166 (112–235)
$\Delta$ NEE	12 (7–18)	16 (9–26)	5 (3–8)	33 (19–52)
Total	32 (24–40)	163 (104–239)	5 (3–8)	199 (131–288)

381 Australia (145.5–154.5 E, 28.5–38.5 S). We divide forests into burned and unburned re-  
 382 gions using a threshold of 50 gC m<sup>-2</sup> of biomass burning emissions over the 2019–2020  
 383 growing season for each 0.1° × 0.1° grid cell. For non-forested regions, GPP was sup-  
 384 pressed during Oct–Jan (54% below mean), but rapidly recovered to above average when  
 385 cooler-wetter conditions dominate (33% above mean for Feb–May). In the unburned forested  
 386 regions, GPP was suppressed during Oct–Jan (23% below mean), with a partial recov-  
 387 ery during Feb–May (8% below mean). In contrast, the burned forests showed a larger  
 388 reduction in GPP during Oct–Jan (37% below mean) that persisted throughout Feb–  
 389 May (31% below mean). Similar reductions are found for MODIS near-infrared reflectance  
 390 of terrestrial vegetation (NIR<sub>V</sub>) and solar induced fluorescence (SIF) measurements from  
 391 TROPOMI and OCO-2 for these vegetation types (see Text S3. and Figure S5 in the  
 392 supporting information). The similar reduction in NIR<sub>V</sub> suggest that structural changes  
 393 in vegetation are partially responsible for the reductions in GPP (He et al., 2020; Y. Sun  
 394 et al., 2015; Yoshida et al., 2015), and are consistent with site level observations of fo-  
 395 liar death in eucalypt forests during 2019–2020 (Nolan et al., 2021). In total, 166 TgC

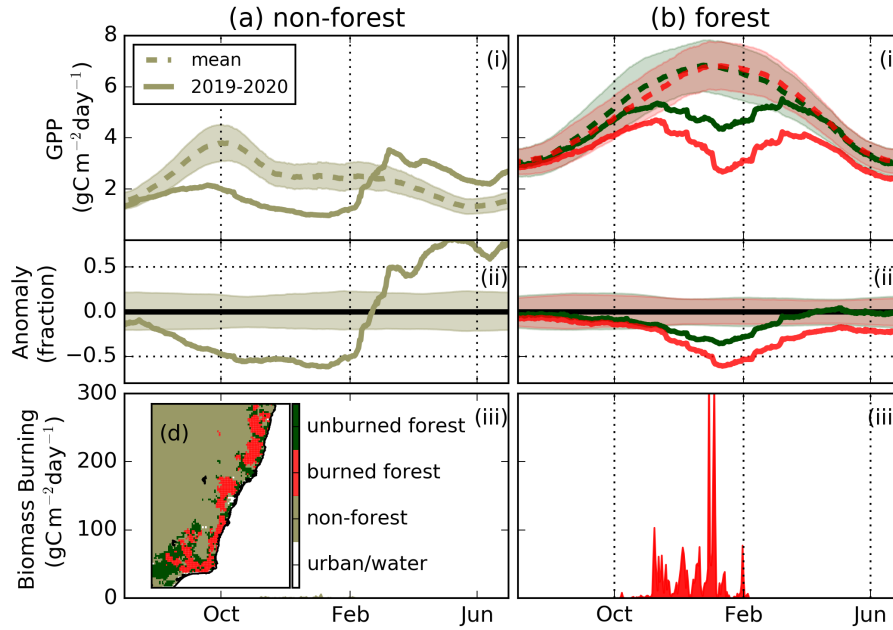


**Figure 6.** Timeseries of (i) GPP, (ii) anomaly in GPP as a fraction of the mean and (iii) biomass burning emissions for (a) non-forest (combined Crop-land/Grassland/Savanna/Shrubland) and (b) unburned and burned forest. (d) The spatial extent of non-forest, and burned and unburned forest over southeast Australia (145.5–154.5 E, 28.5–38.5 S).

396 (range: 113–236 TgC) of  $\text{CO}_2$  was released through biomass burning and 33 TgC (range:  
397 19–52 TgC) was released due to anomalies in NEE over Oct–May (Table 3).

## 398 5 Impact of 2019–2020 anomalies on the regional carbon budget

399 To contextualize the carbon loss over the 2019–2020 growing season, it is useful to  
400 compare this period to the long term mean. Here, we compare the estimated net bio-  
401 sphere exchange (NBE, sum of NEE and biomass burning) for 2019–2020 relative to  $\text{CO}_2$   
402 flux inversions spanning the 2010–2019 growing seasons. For simplicity, we will refer to  
403 growing seasons as  $\text{YY}_1/\text{YY}_2$  (e.g., “19/20”), which encompass July of  $\text{YY}_1$  through June  
404 of  $\text{YY}_2$ .

405 We examine annual net NBE from the “GOSAT+surface+TCCON” flux inversion  
406 by Byrne, Liu, Lee, et al. (2020) (spanning 2010–2015) and the IS+LNLGOG inversion  
407 (spanning 2015–2019) described in Sec. 3.2. Figure 7 shows NBE estimates for southeast  
408 Australia over the 10/11 through 19/20 period. We find that the magnitude of the 19/20  
409 NBE anomaly (mean: 186  $\text{TgC year}^{-1}$ , range: 118 to 275  $\text{TgC year}^{-1}$ ) significantly ex-  
410 ceeds NBE variability over the 10/11 to 18/19 period, confirming the extreme magni-  
411 tude of this event. The mean annual net NBE sink over 10/11–18/19 is found to be -  
412 9.5  $\text{TgC year}^{-1}$  (range: -16.1 to -3.4  $\text{TgC year}^{-1}$ ). However, this mean value is a small  
413 residual of considerable inter-annual variations (standard deviation of 40  $\text{TgC year}^{-1}$ ),  
414 ranging from sink of -73  $\text{TgC year}^{-1}$  (range: -114 to -41  $\text{TgC year}^{-1}$ ) in 10/11, driven  
415 by a strong La Niña (Poulter et al., 2014), to a source of 57  $\text{TgC year}^{-1}$  (range: 28 to  
416 99  $\text{TgC year}^{-1}$ ) during the 18/19 drought. The magnitude of interannual variations in

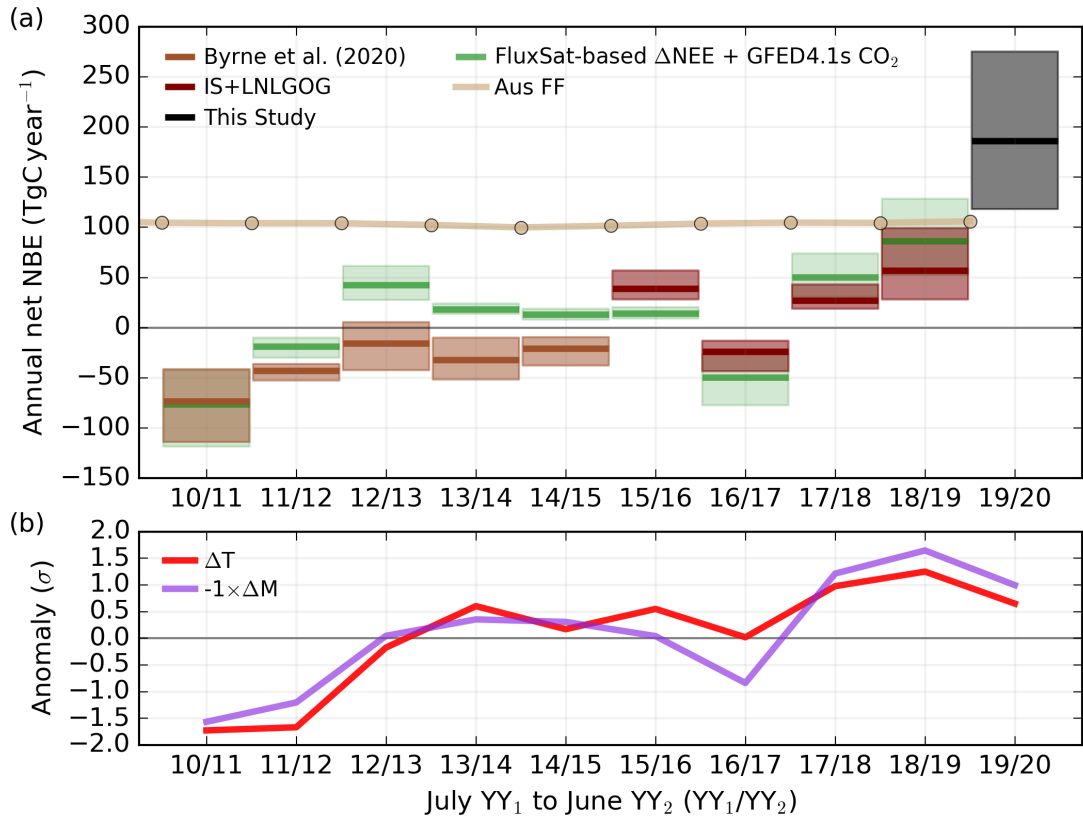


**Figure 7.** (a) Annual (July-June) net NBE from 10/11 to 19/20 over southeast Australia (142.5–157.5 E, 28–40 S). Flux inversion NBE results are shown for Byrne, Liu, Lee, et al. (2020) (spanning 10/11 to 14/15) and IS+LNLGOG (spanning 15/16 to 18/19), where the solid line shows the mean and the spread shows the range of estimates obtained using three different priors. FluxSat-based NBE anomalies also shown, and are based on the regressions presented in Sec. 3.3. For comparison, the IEA Fossil fuel emissions for all of Australia are also plotted. (b) Standard deviations of anomalies for ERA5 soil temperature and soil moisture over southeast Australia relative to a 10/11 to 18/19 baseline.



**Table 4.** Estimates of 2019–2020 CO<sub>2</sub> biomass burning emissions.

source	best (TgC)	range (TgC)
GFED4.1s	132	
FullCAM <sup>a</sup>	232 <sup>b</sup>	
D. M. J. S. Bowman, Williamson, Price, et al. (2020)	184 <sup>b</sup>	85–282
Shiraishi and Hirata (2021)	147 <sup>c</sup>	141–153 <sup>d</sup>
GFASv1.2	55	
This study	167	113–236

<sup>a</sup>Australian Government Department of Industry and Resources (2020)

<sup>b</sup>Australian temperate zone.

<sup>c</sup>Oct-Feb in New South Whales and Victoria.

<sup>d</sup>1 $\sigma$  uncertainty, propagated in quadrature.

417 NBE are independently confirmed by FluxSat-based  $\Delta$ NEE (calculated using the regres-  
418 sions from Sec. 3.3).

419 Interannual variations in NBE are found to be closely associated with climate vari-  
420 ability. Strong correlations are obtained with soil temperature and moisture for the flux  
421 inversions ( $R^2=0.69/0.69$  for temp/moist) and FluxSat-based  $\Delta$ NBE ( $R^2=0.60/0.87$  for  
422 temp/moist). We further examine the relationship between climate variability and up-  
423 take over the 18 year period covering 01/02–18/19 for both forests and non-forests with  
424 FluxSat GPP (Fig. S7). Over this longer period, we find that soil moisture variability  
425 is strongly correlated with variability in FluxSat GPP for forests ( $R^2 = 0.77$ ) and non-  
426 forests ( $R^2 = 0.88$ ). However, soil temperature is not correlated with GPP for forests  
427 ( $R^2 = 0.06$ ) and moderately correlated with non-forests ( $R^2 = 0.57$ ), suggesting that  
428 moisture availability is the primary driver of interannual variations in productivity.

429 This relationship between carbon uptake and climate variability has significant im-  
430 plications for the recovery of these ecosystems. The rate at which the 19/20 carbon loss  
431 will be re-absorbed may depend strongly on climate variability and change. Based on  
432 the mean NBE estimate of  $-9.5 \text{ TgC year}^{-1}$  (range:  $-16.1$  to  $-3.4 \text{ TgC year}^{-1}$ ) over 10/11  
433 to 18/19, we would expect an anomalous carbon release of  $199 \text{ TgC year}^{-1}$  (range:  $131$ –  
434  $288 \text{ TgC year}^{-1}$ ) to be recovered in  $\sim 21$  years (range: 8–85 years). However, having ideal  
435 cool-wet conditions like 10/11 could shorten this to six years, while hot-dry conditions  
436 could prevent a full recovery indefinitely. This highlights the importance of both quan-  
437 tifying the sensitivity of these ecosystems to climate variability, and accurately project-  
438 ing regional climate changes for predicting the recovery of these ecosystems.

## 439 6 Discussion

### 440 6.1 Comparison of biomass burning estimates with other studies

441 Previous estimates of the 2019–2020 Australian biomass burning CO<sub>2</sub> emissions  
442 have been derived using bottom-up methods. Most of these estimates are based on burned  
443 area, wherein, trace gas emissions are derived from space-based burned area measure-  
444 ments using estimate of fire severity, type of vegetation, mass of fuel and trace gas emis-  
445 sion factors (Australian Government Department of Industry & Resources, 2020; D. M. J. S. Bow-  
446 man, Williamson, Price, et al., 2020; Shiraishi & Hirata, 2021). In addition, GFAS uses

447 an alternative bottom-up approach by estimating emissions based on MODIS fire radiative  
448 power observations and trace gas emission factors.

449 The emission estimates calculated in this study are “top-down”, in that they are  
450 based on observations of the emitted trace gases in the atmosphere. Thus, the differences  
451 in approach are complementary, and consistency between top-down and bottom-up es-  
452 timates provides increased confidence in emission estimates. Our estimate of CO<sub>2</sub> emis-  
453 sions overlaps with all existing burned-area-based estimates of biomass burning CO<sub>2</sub> over  
454 southeast Australia (Table 4), providing increased confidence in these estimates. How-  
455 ever, our estimated range suggests larger emissions than provided by the GFAS radiative-  
456 power-based method, suggesting the GFAS underestimates biomass burning over south-  
457 east Australia during 2019–2020.

## 458 6.2 Implications for southeast Australia

459 The 2019–2020 carbon loss of 199 TgC (range: 131–288 TgC) significantly exceeds  
460 annual CO<sub>2</sub> flux anomalies of any year since 2010 ( $\sim 5\sigma$  anomaly) and exceeds total an-  
461 nual Australian fossil fuel emissions (2010–2019 average of 104 TgC year<sup>-1</sup>). This demon-  
462 strates the impact that extreme events can have on the regional carbon budget, and sug-  
463 gests changes in the frequency of extreme heat, fire weather and drought could have a  
464 strong impact on the regional carbon balance.

465 During the study period, there was a robust recovery for unburned ecosystems, sug-  
466 gesting that drought- and heat-induced carbon losses over southeast Australia will be  
467 rapidly re-absorbed. This is consistent with recent modeling work suggesting resilience  
468 to drought in southeast Australian forests (De Kauwe et al., 2020). However, this rapid  
469 recovery may be unusual, due to heavy rainfall and below average temperatures during  
470 the autumn, which strongly modulate productivity in dryland ecosystems (Huxman et  
471 al., 2004; Haverd et al., 2017). Furthermore, there may be drought-induced damages to  
472 these ecosystems that are not captured in this analysis, such as drought-induced tree mor-  
473 tality, which has the potential to impact species and biomass composition (Batllori et  
474 al., 2020; Burton et al., 2021; Fensham et al., 2019). Recovery in burned ecosystems was  
475 much more muted, consistent with major structural damage, preventing a rapid recov-  
476 ery when favorable conditions return.

477 For the years ahead, the speed and extent of carbon uptake will depend strongly  
478 on the climate conditions. The top-down 2010–2019 mean annual sink of -9.5 TgC year<sup>-1</sup>  
479 (range: -16.1 to -3.4 TgC year<sup>-1</sup>) suggests that a full recovery of carbon pools will take  
480 21 years (range: 8–85 years). However, the regional net annual flux showed large inter-  
481 annual variations closely linked with variability in temperature and moisture, with cooler-  
482 wetter years being associated with increased uptake. This is consistent with site-level  
483 observations showing that rainfall is an important driver of the rate of biomass recov-  
484 ery (Volkova et al., 2019; Q. Sun et al., 2020). Under cool-wet conditions, similar to the  
485 2010–2011 La Nina event, carbon recovery could be rapid (within a decade). However,  
486 if conditions are warm and dry, which are expected to become more frequent with cli-  
487 mate change (Perkins-Kirkpatrick & Gibson, 2017; Abatzoglou et al., 2019), carbon re-  
488 recovery could last indefinitely. Further, possible recurrent fires could act to significantly  
489 lengthen the recovery period.

490 In addition to the carbon sequestration, it is important to consider ecosystem re-  
491 covery. Severe fires can have legacy impacts on ecosystem function even after carbon stocks  
492 have been largely regenerated. Severe fires in Eucalyptus forests have been shown to in-  
493 clude persistent changes to canopy structure (Karna et al., 2019), increase tree mortal-  
494 ity (Bennett et al., 2016; Etchells et al., 2020) and cause changes in understory compo-  
495 sition and structure (D. M. J. S. Bowman et al., 2014; Fairman et al., 2016; Pellegrini  
496 et al., 2021; Fletcher et al., 2014). In particular, fire induced tree mortalities are gen-  
497 erally higher in smaller-younger cohorts (Bennett et al., 2016; Bowd et al., 2021). For

498 some species, such as Mountain Ash, extended periods of  $\sim 20$  years are required mature  
 499 and produce viable seeds (Lindenmayer et al., 2021), potentially leaving these ecosys-  
 500 tems vulnerable to recurrent fire for several decades.

501 Finally, the impact of disturbance and ecosystem recovery should be considered within  
 502 the context of ongoing climate change. This region is experiencing more frequent extreme  
 503 heat and fire events (Abram et al., 2020; Sharples et al., 2016; Bradstock et al., 2014),  
 504 a trend that is expected to continue with climate change (Perkins-Kirkpatrick & Gib-  
 505 son, 2017; Abatzoglou et al., 2019; Dowdy et al., 2019; Di Virgilio et al., 2019; Herold  
 506 et al., 2021). Projections of regional trends in drought are less certain. However, sev-  
 507 eral studies suggest drought intensity and frequency may increase in the coming years  
 508 over much of southeast Australia (Ukkola et al., 2020; Kirono et al., 2020; Herold et al.,  
 509 2021; J. Wang et al., 2021), with Herold et al. (2021) finding 1-in-20 year droughts may  
 510 become 1-in-5 year events by 2060–2079.

511 These trends in climate variability will likely have a number of impacts on the car-  
 512 bon cycle of the region. A shortening inter-fire interval will increase the risk of recur-  
 513 rent fire across much of southeast Australia. Repeat fires during the recovery period from  
 514 the previous fire are a major risk for forest ecosystems, with studies finding significant  
 515 negative impacts on ecosystem function for both obligate seeder (D. M. J. S. Bowman  
 516 et al., 2014) and resprouter-dominated communities (Fairman et al., 2017; Collins, Hunter,  
 517 et al., 2021). This risk may be compounded by longer recovery periods after fire due to  
 518 frequent extreme heat and drought events. In particular, if the inter-fire interval decreases  
 519 below the recovery time, permanent carbon loss will be experienced by these ecosystems,  
 520 potentially leading to major changes in the ecosystem structure and fire regimes of the  
 521 region (Boer et al., 2016).

522 Detecting permanent changes in the regional carbon budget will require sustained  
 523 monitoring of the regional carbon budget through a combination of expanding top-down  
 524 constraints (Crisp et al., 2018), as presented in this work, in addition to continued and  
 525 improved site-level monitoring (D. M. J. S. Bowman, Williamson, Yebra, et al., 2020).

### 526 **6.3 Uncertainties in estimating carbon flux**

527 In this analysis, we have calculated drought-induced NEE anomalies and biomass  
 528 burning  $\text{CO}_2$  anomalies over southeast Australia during 2019–2020 that are consistent  
 529 with observed  $X_{\text{CO}}$ ,  $X_{\text{CO}_2}$  and FluxSat GPP. Still, there are remaining challenges in quan-  
 530 tifying carbon cycle perturbations, leading to large uncertainties in the estimates pre-  
 531 sented here.

#### 532 **6.3.1 Model transport**

533 Accurate representation of atmospheric transport of CO and  $\text{CO}_2$  from biomass  
 534 burning remains a major challenge (Eastham & Jacob, 2017). Rapid pyroconvective mo-  
 535 tions are not well represented in our model simulations. This leads to errors in simulated  
 536  $X_{\text{CO}}$  fields relative to the observations and systematic errors in flux inversions. In our  
 537 analysis, we performed sensitivity analyses by evaluating the posterior CO fields for emis-  
 538 sions released at the surface and at an estimated plume injection height (emitted at up  
 539 to 6 km in altitude, Text S1 and Figure S1 of the supporting information), and found  
 540 that the posterior emissions better matched independent CO observations in both cases.  
 541 Still, Modeled CrIS  $X_{\text{CO}}$ , which are most sensitive to the upper troposphere, showed weak  
 542 sensitivity to biomass burning emissions despite the fact that biomass burning species  
 543 were observed in the stratosphere (Khaykin et al., 2020; Schwartz et al., 2020; Hirsch &  
 544 Koren, 2021). This suggests that modeled vertical motions are too weak and do not fully  
 545 capture the vertical structure of biomass burning species produced by strong pyrocon-  
 546 vective motions. Such systematic errors are challenging to address, but one possible av-

547 enue of future study would be to utilize weak constraint 4D-Var (Stanevich et al., 2019),  
 548 which would allow for optimizing both surface fluxes and the atmospheric state. Account-  
 549 ing for the total CO change throughout the column would provide a quantitative assess-  
 550 ment of the impact of systematic transport errors on CO emission estimates. Another  
 551 avenue of future work could be to improve the representation of pyroconvective motions  
 552 in transport models. As these motions are sub-grid scale for typical chemical transport  
 553 models, this would most likely require prescribing vertical mass fluxes calculated by a  
 554 high-resolution cloud resolving model.

### 555 **6.3.2 $CO_2/CO$ emission ratio**

556 To estimate biomass burning  $CO_2$  emissions from estimated CO emissions, the  $CO_2/CO$   
 557 emission ratio needs to be precisely and accurately known. However, there is consider-  
 558 able uncertainty in this value, with recent reported values for Australian forests rang-  
 559 ing from  $8.59 \pm 1.16 \text{ gC gC}^{-1}$  (Paton-Walsh et al., 2014) to  $12.65 \pm 2.34 \text{ gC gC}^{-1}$  (Guérette  
 560 et al., 2018) (Table S7). We incorporated some of this uncertainty by applying differ-  
 561 ent emission ratios for the GFAS ( $9.44 \text{ gC gC}^{-1}$  for forests) and GFED ( $11.91 \text{ gC gC}^{-1}$   
 562 for forests) based biomass burning estimates. Comparison of simulated and measured  
 563  $X_{CO_2}$  and  $X_{CO}$  retrievals at Wollongong and Lauder supports the emission ratios em-  
 564 ployed here (Fig. S8). For Wollongong, we found an observed  $X_{CO_2}/X_{CO}$  ratio of  $0.014 \text{ ppm ppb}^{-1}$   
 565 (range:  $0.011$  to  $0.036 \text{ ppm ppb}^{-1}$ ) and a simulated  $X_{CO_2}/X_{CO}$  ratio of  $0.017 \text{ ppm ppb}^{-1}$   
 566 (range:  $0.009$  to  $0.021 \text{ ppm ppb}^{-1}$ ), while the dynamic range of biomass-burning-impacted  
 567 measurements at Lauder was not sufficient to provide a strong constraint on the emis-  
 568 sion ratio (note that  $X_{CO_2}/X_{CO}$  ratios are not directly comparable to emission ratios due  
 569 to chemical loss of CO). Still, we acknowledge that uncertainty in the  $CO_2/CO$  emis-  
 570 sion ratio remains a major challenge in estimating  $CO_2$  biomass burning emissions from  
 571 CO flux inversion analyses.

### 572 **6.3.3 Data Gaps**

573 It is also notable that the largest biomass burning enhancements of  $X_{CO_2}$  were not  
 574 observable by OCO-2 or TCCON sites due to the presence of co-emitted aerosols (J. Wang  
 575 et al., 2020). Rapid deployment of aircraft campaigns that observe the chemical com-  
 576 position of the biomass burning plumes would help mitigate these sampling biases. The  
 577 serendipitous occurrence of the Atmospheric Carbon and Transport – America (ACT-  
 578 America) flight campaign during the 2019 Midwest floods provided supporting evidence  
 579 of the flood-induced  $CO_2$  flux anomalies estimated by Yin, Byrne, et al. (2020), result-  
 580 ing in increased confidence in those estimates.

### 581 **6.3.4 Estimating $\Delta NEE$**

582 Due to atmospheric mixing and the relatively sparse sampling of  $X_{CO_2}$  by OCO-  
 583 2, it is not possible to fully resolve the spatial and temporal structure in  $\Delta NEE$ . Thus,  
 584 we utilized the spatiotemporal structure of  $\Delta GPP$  to predict the spatiotemporal struc-  
 585 ture of  $\Delta NEE$  for forests and non-forest to regularize the problem. Although, this lin-  
 586 ear relationship is generally supported by eddy-covariance measurements within Aus-  
 587 tralia (Li et al., 2017), there are likely many cases where this linearity breaks down. We  
 588 do not account for this source of systematic error in our analysis, suggesting that the un-  
 589 certainties may be larger and more systematic than estimated here.

### 590 **6.3.5 Unaccounted for carbon fluxes**

591 Finally, we note that we only quantify land-atmosphere  $CO_2$  fluxes in this study,  
 592 and that a full accounting of the carbon stock changes due to this event would need to  
 593 incorporate lateral carbon fluxes. Intense rainfall following immediately after fire likely

594 increased runoff of ash and debris to waterways, leading to a number of record fish kills  
 595 in estuarine sites located downstream of burned areas (Silva et al., 2020). Thus, there  
 596 may have been considerable export of carbon to waterways and the ocean, but this has  
 597 not been quantified to our knowledge. In addition, we only include estimates of biomass  
 598 burning emissions of CO<sub>2</sub>. We estimate and additional 15–29 TgC emitted as CO from  
 599 biomass burning.

## 600 7 Conclusions

601 Extreme events play a major role in the carbon cycling of ecosystems, but quan-  
 602 tifying the impact of these events on the carbon budget remains challenging. Incorpor-  
 603 ating a variety of space-based observations, we have provided a comprehensive account-  
 604 ing of biosphere-atmosphere CO<sub>2</sub> flux anomalies due to drought, heat, and fire over south-  
 605 east Australia (145.5–154.5 E, 28.5–38.5 S) during the 2019–2020 austral growing sea-  
 606 son. In total, biomass burning released 113–236 TgC of CO<sub>2</sub> and anomalies in Oct–May  
 607 NEE reduced carbon uptake by 19–52 TgC. Carbon losses were found to be most severe  
 608 in forested regions and were dominated by biomass burning emissions. Unburned forests  
 609 and non-forest ecosystems recovered to mean or greater productivity when cooler-wetter  
 610 conditions dominated during the late austral summer and autumn, however, primary pro-  
 611 ductivity remained suppressed in burned regions.

612 The carbon loss over 2019–2020 is found to significantly exceed interannual vari-  
 613 ability in the regional carbon uptake over 2010–2019 from a set of top-down estimates  
 614 ( $\sim 5\sigma$  anomaly), highlighting the extreme nature of this event. In the years to come,  
 615 these ecosystems are expected to largely recover lost carbon stocks. However, the speed  
 616 of recovery may be strongly regulated by climate variability and change, with reduced  
 617 uptake during hot and dry conditions. This has important implications for the future  
 618 carbon budget of the region. Climate-change-driven increases in the frequency of extreme  
 619 heat and drought events will increase the recovery period after fires and decrease the inter-  
 620 fire interval. If the recovery period becomes longer than the inter-fire interval then per-  
 621 manent carbon losses are likely.

622 This analysis finds that space-based remote sensing of trace gases and MODIS re-  
 623 flectances provide strong constraints on carbon cycle anomalies produced by extreme events.  
 624 Still, there are remaining challenges that result in significant uncertainties in inferred fluxes.  
 625 For inferring biomass burning estimates from X<sub>CO</sub> measurements, resolving pyroconvec-  
 626 tive tracer transport remains a major challenge and source of uncertainty. Aerosols co-  
 627 emitted with biomass burning CO and CO<sub>2</sub> prevent total-column trace gas retrievals within  
 628 much of the biomass burning plume. In addition, estimating CO<sub>2</sub> emissions from CO  
 629 has considerable uncertainty, as does estimating the spatiotemporal structure of  $\Delta$ NEE  
 630 estimates. Addressing these sources of uncertainty, in addition to expanding space-based  
 631 trace gas observations will provide increasingly precise estimates of carbon release from  
 632 extreme events.

## 633 Appendix A Flux inversion configuration

634 The nested CO flux inversions are performed over a one-way nested domain of (100°–  
 635 177.5° E, 0° – 60° S) at 0.5°×0.625° spatial resolution. Assimilated TROPOMI X<sub>CO</sub>  
 636 super-obs are generated by aggregating measurements with the quality flag  $\geq 0.5$  to the  
 637 0.5°×0.625° spatial grid. The flux inversions optimize scaling factors to each model grid-  
 638 cell for prior biomass burning emissions from 5 Nov 2019 through 14 Jan 2020. Prior biomass  
 639 burning emissions vary between flux inversions and are listed in Table 1. For the anthro-  
 640 pogenic emissions, we combine off-line emission inventories from the EDGAR 4.2 global  
 641 model (Olivier & Berdowski, 2001) and several regional models including the US Envi-  
 642 ronmental Protection Agency (EPA) National Emission Inventory (NEI) for 2008 in North  
 643 America, the Criteria Air Contaminants (CAC) inventory for Canada, the Big Bend Re-

644 gional Aerosol and Visibility Observational (BRAVO) Study Emissions Inventory for Mex-  
 645 ico (Kuhns et al., 2003), the Cooperative Program for Monitoring and Evaluation of the  
 646 Long-range Transmission of Air Pollutants in Europe (EMEP) inventory for Europe in  
 647 2000 (Vestreng, 2002) and the Streets Asia emissions inventory for 2000 (Streets et al.,  
 648 2006). Monthly BioFuel emissions are from the Emission Database for Global Atmospheric  
 649 Research (EDGAR) (Crippa et al., 2016), monthly shipping emissions from the Inter-  
 650 national Comprehensive Ocean–Atmosphere Data Set (ICOADS) (C. Wang et al., 2008),  
 651 and hourly Biogenic emissions from Model of Emissions of Gases and Aerosols from Na-  
 652 ture (MEGAN) (Guenther et al., 2012).

653 Boundary conditions for the nested flux inversions are generated by performing a  
 654 global inversion with GHGF-Flux at  $4^\circ \times 5^\circ$  spatial resolution over the three month pe-  
 655 riod from November 2019 through January 2020. The global inversion assimilates TROPOMI  
 656  $X_{CO}$  super-obs (aggregated to  $4^\circ \times 5^\circ$  for measurements with quality flag equal to one)  
 657 to optimize 14-day scale factors for prior GFED biomass burning emissions at each grid  
 658 cell. Other prescribed emissions are identical to the nested flux inversion. Initial con-  
 659 ditions for the global flux inversion are obtained from a global MOPITT  $X_{CO}$  flux in-  
 660 version. To test the sensitivity of inferred fluxes to the boundary conditions on the nested  
 661 flux inversions, we generate a second set of boundary conditions that are identical to those  
 662 from the global TROPOMI flux inversion but have CO increased by 10 ppb at all times  
 663 and locations.

## 664 Acknowledgments

665 BB was supported by an appointment to the NASA Postdoctoral Program at the  
 666 Jet Propulsion Laboratory, administered by Universities Space Research Association un-  
 667 der contract with NASA. BB and JL were supported by the NASA OCO2/3 science team  
 668 program NNH17ZDA001N-OCO2. KWB was supported by the NASA Carbon Monitor-  
 669 ing System (CMS) project (NNH16ZDA001N-CMS). JJ was supported by the NASA Mak-  
 670 ing Earth System Data Records for Use in Research Environments (MEaSUREs) and  
 671 Arctic Boreal Vulnerability Experiment (ABOVE) programs. The research carried out  
 672 at the Jet Propulsion Laboratory, California Institute of Technology, was under a con-  
 673 tract with the National Aeronautics and Space Administration. Resources supporting  
 674 this work were provided by the NASA High-End Computing (HEC) Program through  
 675 the NASA Advanced Supercomputing (NAS) Division at Ames Research Center. ODIAC  
 676 project is supported by Greenhouse Gas Observing SATellite (GOSAT) project, National  
 677 Institute for Environmental Studies (NIES), Japan. Wollongong TCCON measurements  
 678 over the period of this study are supported by the Australian Research Council (ARC)  
 679 grants DP160101598 and LE0668470, while NMD is supported by an ARC Future Fel-  
 680 lowship, FT180100327.

681 GFED data were downloaded from <https://www.globalfiredata.org/>. GFAS data  
 682 were downloaded from <https://apps.ecmwf.int/datasets/>. GFAS is generated using Coper-  
 683 nicus Atmosphere Monitoring Service Information 2020, neither the European Commis-  
 684 sion nor ECMWF is responsible for any use that may be made of the information it con-  
 685 tains. TCCON data were obtained from the TCCON Data Archive, hosted by Caltech-  
 686 DATA (<https://tccodata.org>). We downloaded version 9 of the ACOS OCO-2 lite files  
 687 from the CO<sub>2</sub> Virtual Science Data Environment (<https://CO2.jpl.nasa.gov/>). OCO-2  
 688 data were produced by the OCO-2 project at the Jet Propulsion Laboratory, California  
 689 Institute of Technology, and obtained from the OCO-2 data archive maintained at the  
 690 NASA Goddard Earth Science Data and Information Services Center. FluxSat data were  
 691 downloaded from [https://avdc.gsfc.nasa.gov/pub/tmp/FluxSat\\_GPP/](https://avdc.gsfc.nasa.gov/pub/tmp/FluxSat_GPP/). MODIS land cover  
 692 data was downloaded from the EOSDIS Land Processes DAAC. ETOPO1 elevation data  
 693 was downloaded from <https://www.ngdc.noaa.gov>. ERA5-Land data are obtained from  
 694 the Climate Data Store (<https://cds.climate.copernicus.eu>). TROPOMI CO data were  
 695 downloaded from <http://www.tropomi.eu/data-products/carbon-monoxide>. CrIS CO is

696 provided by the NASA TROPOspheric Ozone and its Precursors from Earth System Sound-  
 697 ing (TROPESS) and available from <https://tes.jpl.nasa.gov>. MODIS NIRv was calcu-  
 698 lated from MODIS NBAR measurements (MCD43A4), which were downloaded from the  
 699 LP DAAC. TROPOMI L2 SIF data were downloaded from <ftp://fluo.gps.caltech.edu/data/tropomi/ungridded/SI>  
 700 OCO-2 L2 SIF data are available from the GES DISC (<https://disc.gsfc.nasa.gov>). Bar-  
 701 ring Head CO/CO<sub>2</sub> and Lauder CO data were downloaded from the World Data Cen-  
 702 tre for Greenhouse Gases (<https://gaw.kishou.go.jp/>). Lauder CO<sub>2</sub> data were obtained  
 703 from the site PIs. Paul Krummel, Ray Langenfelds and Zoe Loh are thanked for sup-  
 704 plying the Cape Grim CO/CO<sub>2</sub> data. The grided daily estimates of  $\Delta$ NEE and biomass  
 705 burning will be made publicly available upon publication. The authors would like to thank  
 706 Tom Oda for guidance on fossil fuel statistics. We thank the editor and reviewers for valu-  
 707 able comments that greatly improved this study.

708 ©2021. All rights reserved.

## 709 References

- 710 Abatzoglou, J. T., Williams, A. P., & Barbero, R. (2019). Global emergence of an-  
 711 thropogenic climate change in fire weather indices. *Geophysical Research Let-*  
 712 *ters*, *46*(1), 326–336.
- 713 Abram, N. J., Henley, B. J., Gupta, A. S., Lippmann, T. J., Clarke, H., Dowdy,  
 714 A. J., ... others (2020). Connections of climate change and variability to  
 715 large and extreme forest fires in southeast Australia. *Communications Earth &*  
 716 *Environment*, *2*(1), 1–17.
- 717 Akagi, S. K., Yokelson, R. J., Wiedinmyer, C., Alvarado, M. J., Reid, J. S., Karl, T.,  
 718 ... Wennberg, P. O. (2011). Emission factors for open and domestic biomass  
 719 burning for use in atmospheric models. *Atmospheric Chemistry and Physics*,  
 720 *11*(9), 4039–4072. Retrieved from [https://acp.copernicus.org/articles/](https://acp.copernicus.org/articles/11/4039/2011/)  
 721 [11/4039/2011/](https://acp.copernicus.org/articles/11/4039/2011/) doi: 10.5194/acp-11-4039-2011
- 722 Amante, C., & Eakins, B. W. (2009). ETOPO1 arc-minute global relief model: pro-  
 723 cedures, data sources and analysis.
- 724 Australian Government Department of Industry, E., Science, & Resources. (2020).  
 725 *Estimating greenhouse gas emissions from bushfires in Australia’s temperate*  
 726 *forests: focus on 2019–20*. Retrieved from [https://www.industry.gov.au/](https://www.industry.gov.au/sites/default/files/2020-04/estimating-greenhouse-gas-emissions-from-bushfires-in-Australias-temperate-forests-focus-on-2019-20.pdf)  
 727 [sites/default/files/2020-04/estimating-greenhouse-gas-emissions](https://www.industry.gov.au/sites/default/files/2020-04/estimating-greenhouse-gas-emissions-from-bushfires-in-Australias-temperate-forests-focus-on-2019-20.pdf)  
 728 [-from-bushfires-in-{A}ustralias-temperate-forests-focus-on-2019-20](https://www.industry.gov.au/sites/default/files/2020-04/estimating-greenhouse-gas-emissions-from-bushfires-in-Australias-temperate-forests-focus-on-2019-20.pdf)  
 729 [.pdf](https://www.industry.gov.au/sites/default/files/2020-04/estimating-greenhouse-gas-emissions-from-bushfires-in-Australias-temperate-forests-focus-on-2019-20.pdf)
- 730 Bastos, A., Gouveia, C., Trigo, R., & Running, S. W. (2014). Analysing the spatio-  
 731 temporal impacts of the 2003 and 2010 extreme heatwaves on plant productiv-  
 732 ity in europe. *Biogeosciences*, 3421–3435.
- 733 Batllori, E., Lloret, F., Aakala, T., Anderegg, W. R., Aynekulu, E., Bendixsen,  
 734 D. P., ... others (2020). Forest and woodland replacement patterns following  
 735 drought-related mortality. *Proceedings of the National Academy of Sciences*,  
 736 *117*(47), 29720–29729.
- 737 Bennett, L. T., Bruce, M. J., MacHunter, J., Kohout, M., Tanase, M. A., & Aponte,  
 738 C. (2016). Mortality and recruitment of fire-tolerant eucalypts as influenced by  
 739 wildfire severity and recent prescribed fire. *Forest Ecology and Management*,  
 740 *380*, 107–117.
- 741 Boer, M. M., Bowman, D. M. J. S., Murphy, B. P., Cary, G. J., Cochrane, M. A.,  
 742 Fensham, R. J., ... others (2016). Future changes in climatic water bal-  
 743 ance determine potential for transformational shifts in Australian fire regimes.  
 744 *Environmental Research Letters*, *11*(6), 065002.
- 745 Boer, M. M., de Dios, V. R., & Bradstock, R. A. (2020). Unprecedented burn area  
 746 of Australian mega forest fires. *Nature Climate Change*, *10*(3), 171–172.
- 747 Borsdorff, T., Aan de Brugh, J., Hu, H., Aben, I., Hasekamp, O., & Landgraf, J.

- 748 (2018). Measuring carbon monoxide with TROPOMI: First results and a com-  
 749 parison with ECMWF-IFS analysis data. *Geophysical Research Letters*, *45*(6),  
 750 2826–2832.
- 751 Bowd, E. J., Blair, D. P., & Lindenmayer, D. B. (2021). Prior disturbance legacy ef-  
 752 fects on plant recovery post-high-severity wildfire. *Ecosphere*, *12*(5), e03480.
- 753 Bowman, D. M. J. S. (2000). *Australian rainforests: islands of green in a land of*  
 754 *fire*. Cambridge University Press.
- 755 Bowman, D. M. J. S., Balch, J. K., Artaxo, P., Bond, W. J., Carlson, J. M.,  
 756 Cochrane, M. A., . . . Harrison, S. P. (2009). Fire in the earth system. *Science*,  
 757 *324*(5926), 481–484.
- 758 Bowman, D. M. J. S., Murphy, B. P., Neyland, D. L., Williamson, G. J., & Prior,  
 759 L. D. (2014). Abrupt fire regime change may cause landscape-wide loss of  
 760 mature obligate seeder forests. *Global Change Biology*, *20*(3), 1008–1015.
- 761 Bowman, D. M. J. S., Williamson, G., Yebra, M., Lizundia-Loiola, J., Pettinari,  
 762 M. L., Shah, S., . . . Chuvieco, E. (2020). *Wildfires: Australia needs national*  
 763 *monitoring agency*. Nature Publishing Group.
- 764 Bowman, D. M. J. S., Williamson, G. J., Gibson, R. K., Bradstock, R. A., &  
 765 Keenan, R. J. (2021). The severity and extent of the Australia 2019–20  
 766 eucalyptus forest fires are not the legacy of forest management. *Nature Ecology*  
 767 *& Evolution*, 1–8.
- 768 Bowman, D. M. J. S., Williamson, G. J., Price, O. F., Ndalila, M. N., & Bradstock,  
 769 R. A. (2020). Australian forests, megafires and the risk of dwindling carbon  
 770 stocks. *Plant, Cell & Environment*.
- 771 Bowman, K. W., Rodgers, C. D., Kulawik, S. S., Worden, J., Sarkissian, E., Oster-  
 772 man, G., . . . others (2006). Tropospheric emission spectrometer: Retrieval  
 773 method and error analysis. *IEEE Transactions on Geoscience and Remote*  
 774 *Sensing*, *44*(5), 1297–1307.
- 775 Bradstock, R., Penman, T., Boer, M., Price, O., & Clarke, H. (2014). Divergent  
 776 responses of fire to recent warming and drying across south-eastern Australia.  
 777 *Global change biology*, *20*(5), 1412–1428.
- 778 Bureau of Meteorology. (2020). *Annual climate statement 2019*. Retrieved from  
 779 <http://www.bom.gov.au/climate/current/annual/aus/#tabs=Overview>
- 780 Burrows, G. (2002). Epicormic strand structure in angophora, eucalyptus and  
 781 lophostemon (myrtaceae): implications for fire resistance and recovery. *New*  
 782 *Phytologist*, 111–131.
- 783 Burton, J. E., Bennett, L. T., Kasel, S., Nitschke, C. R., Tanase, M. A., Fairman,  
 784 T. A., . . . Aponte, C. (2021). Fire, drought and productivity as drivers of dead  
 785 wood biomass in eucalypt forests of south-eastern Australia. *Forest Ecology*  
 786 *and Management*, *482*, 118859.
- 787 Byrne, B., Jones, D. B. A., Strong, K., Polavarapu, S. M., Harper, A. B., Baker,  
 788 D. F., & Maksyutov, S. (2019). On what scales can GOSAT flux inversions  
 789 constrain anomalies in terrestrial ecosystems? *Atmos. Chem. Phys.*, *19*(20),  
 790 13017–13035. Retrieved from [https://www.atmos-chem-phys.net/19/13017/](https://www.atmos-chem-phys.net/19/13017/2019/)  
 791 2019/ doi: 10.5194/acp-19-13017-2019
- 792 Byrne, B., Liu, J., Bloom, A. A., Bowman, K. W., Butterfield, Z., Joiner, J., . . .  
 793 Yin, Y. (2020). Contrasting regional carbon cycle responses to seasonal cli-  
 794 mate anomalies across the east-west divide of temperate north america. *Global*  
 795 *Biogeochemical Cycles*, e2020GB006598.
- 796 Byrne, B., Liu, J., Lee, M., Baker, I. T., B, K. W., Deutscher, N. M., . . . Wunch,  
 797 D. (2020). Improved constraints on northern extratropical CO<sub>2</sub> fluxes  
 798 obtained by combining surface-based and space-based atmospheric CO<sub>2</sub>  
 799 measurements. *Journal of Geophysical Research: Atmospheres*, *125*. doi:  
 800 10.1029/2019JD032029
- 801 Ciais, P., Reichstein, M., Viovy, N., Granier, A., Ogee, J., Allard, V., . . . others  
 802 (2005). Europe-wide reduction in primary productivity caused by the heat and



- 803 drought in 2003. *Nature*, 437(7058), 529–533. doi: [https://doi.org/10.1038/](https://doi.org/10.1038/nature03972)  
 804 nature03972
- 805 Collalti, A., & Prentice, I. C. (2019, 05). Is NPP proportional to GPP? Waring’s  
 806 hypothesis 20 years on. *Tree Physiology*, 39(8), 1473–1483. Retrieved from  
 807 <https://doi.org/10.1093/treephys/tpz034> doi: 10.1093/treephys/tpz034
- 808 Collins, L., Bradstock, R. A., Clarke, H., Clarke, M. F., Nolan, R. H., & Penman,  
 809 T. D. (2021). The 2019/2020 mega-fires exposed Australian ecosystems to an  
 810 unprecedented extent of high-severity fire. *Environmental Research Letters*,  
 811 16(4), 044029.
- 812 Collins, L., Hunter, A., McColl-Gausden, S., Penman, T. D., & Zylstra, P. (2021).  
 813 The effect of antecedent fire severity on reburn severity and fuel structure in a  
 814 resprouting eucalypt forest in victoria, Australia. *Forests*, 12(4), 450.
- 815 Cooperative Global Atmospheric Data Integration Project. (2018). *Multi-laboratory*  
 816 *compilation of atmospheric carbon dioxide data for the period 1957-2017;*  
 817 *obspack.CO2\_1\_globalviewplus.v4.1\_2018\_10\_29; noaa earth system research*  
 818 *laboratory, global monitoring division.* doi: 10.25925/20181026
- 819 Crippa, M., Janssens-Maenhout, G., Dentener, F., Guizzardi, D., Sindelarova, K.,  
 820 Muntean, M., ... Granier, C. (2016). Forty years of improvements in euro-  
 821 pean air quality: regional policy-industry interactions with global impacts.  
 822 *Atmospheric Chemistry and Physics*, 16(6), 3825–3841.
- 823 Crisp, D., Meijer, Y., Munro, R., Bowman, K., & Chatterjee, A. (2018). A constella-  
 824 tion architecture for monitoring carbon dioxide and methane from space.
- 825 Crisp, D., Pollock, H. R., Rosenberg, R., Chapsky, L., Lee, R. A. M., Oyafuso,  
 826 F. A., ... Wunch, D. (2017). The on-orbit performance of the orbit-  
 827 ing carbon observatory-2 (oco-2) instrument and its radiometrically cali-  
 828 brated products. *Atmospheric Measurement Techniques*, 10(1), 59–81. Re-  
 829 trieved from <https://amt.copernicus.org/articles/10/59/2017/> doi:  
 830 10.5194/amt-10-59-2017
- 831 Deb, P., Moradkhani, H., Abbaszadeh, P., Kiem, A. S., Engström, J., Keellings, D.,  
 832 & Sharma, A. (2020). Causes of the widespread 2019–2020 Australian bushfire  
 833 season. *Earth’s Future*, e2020EF001671.
- 834 De Boeck, H. J., Dreesen, F. E., Janssens, I. A., & Nijs, I. (2011). Whole-system  
 835 responses of experimental plant communities to climate extremes imposed in  
 836 different seasons. *New Phytologist*, 189(3), 806–817.
- 837 De Kauwe, M. G., Medlyn, B. E., Ukkola, A. M., Mu, M., Sabot, M. E., Pitman,  
 838 A. J., ... others (2020). Identifying areas at risk of drought-induced tree  
 839 mortality across south-eastern australia. *Global Change Biology*, 26(10), 5716–  
 840 5733.
- 841 DeLucia, E. H., Drake, J. E., Thomas, R. B., & Gonzalez-Meler, M. (2007). For-  
 842 est carbon use efficiency: is respiration a constant fraction of gross primary  
 843 production? *Global Change Biology*, 13(6), 1157–1167.
- 844 Denton, E. M., Dietrich, J. D., Smith, M. D., & Knapp, A. K. (2017). Drought  
 845 timing differentially affects above-and belowground productivity in a mesic  
 846 grassland. *Plant Ecology*, 218(3), 317–328.
- 847 Di Giuseppe, F., Rémy, S., Pappenberger, F., & Wetterhall, F. (2018). Using the  
 848 Fire Weather Index (FWI) to improve the estimation of fire emissions from  
 849 fire radiative power (FRP) observations. *Atmospheric Chemistry and Physics*,  
 850 18(8), 5359–5370. Retrieved from [https://acp.copernicus.org/articles/](https://acp.copernicus.org/articles/18/5359/2018/)  
 851 [18/5359/2018/](https://acp.copernicus.org/articles/18/5359/2018/) doi: 10.5194/acp-18-5359-2018
- 852 Di Virgilio, G., Evans, J. P., Blake, S. A., Armstrong, M., Dowdy, A. J., Sharples,  
 853 J., & McRae, R. (2019). Climate change increases the potential for extreme  
 854 wildfires. *Geophysical Research Letters*, 46(14), 8517–8526.
- 855 Dowdy, A. J., Ye, H., Pepler, A., Thatcher, M., Osbrough, S. L., Evans, J. P., ...  
 856 McCarthy, N. (2019). Future changes in extreme weather and pyroconvection  
 857 risk factors for Australian wildfires. *Scientific reports*, 9(1), 1–11.

- 858 Eastham, S. D., & Jacob, D. J. (2017). Limits on the ability of global eule-  
 859 rian models to resolve intercontinental transport of chemical plumes. *At-*  
 860 *mospheric Chemistry and Physics*, *17*(4), 2543–2553. Retrieved from  
 861 <https://acp.copernicus.org/articles/17/2543/2017/> doi: 10.5194/  
 862 acp-17-2543-2017
- 863 Eldering, A., O’Dell, C. W., Wennberg, P. O., Crisp, D., Gunson, M. R., Viatte, C.,  
 864 ... Yoshimizu, J. (2017). The Orbiting Carbon Observatory-2: first 18 months  
 865 of science data products. *Atmospheric Measurement Techniques*, *10*(2), 549–  
 866 563. Retrieved from <https://amt.copernicus.org/articles/10/549/2017/>  
 867 doi: 10.5194/amt-10-549-2017
- 868 Etchells, H., O’Donnell, A. J., McCaw, W. L., & Grierson, P. F. (2020). Fire sever-  
 869 ity impacts on tree mortality and post-fire recruitment in tall eucalypt forests  
 870 of southwest Australia. *Forest Ecology and Management*, *459*, 117850.
- 871 Fairman, T. A., Bennett, L. T., Tupper, S., & Nitschke, C. R. (2017). Frequent  
 872 wildfires erode tree persistence and alter stand structure and initial composi-  
 873 tion of a fire-tolerant sub-alpine forest. *Journal of Vegetation Science*, *28*(6),  
 874 1151–1165.
- 875 Fairman, T. A., Nitschke, C. R., & Bennett, L. T. (2016). Too much, too soon?  
 876 a review of the effects of increasing wildfire frequency on tree mortality and  
 877 regeneration in temperate eucalypt forests. *International Journal of Wildland*  
 878 *Fire*, *25*(8), 831–848.
- 879 Fensham, R. J., Laffineur, B., & Allen, C. D. (2019). To what extent is drought-  
 880 induced tree mortality a natural phenomenon? *Global Ecology and Biogeogra-*  
 881 *phy*, *28*(3), 365–373.
- 882 Fletcher, M.-S., Wood, S. W., & Haberle, S. G. (2014). A fire-driven shift from for-  
 883 est to non-forest: evidence for alternative stable states? *Ecology*, *95*(9), 2504–  
 884 2513.
- 885 Frank, D., Reichstein, M., Bahn, M., Thonicke, K., Frank, D., Mahecha, M. D., ...  
 886 others (2015). Effects of climate extremes on the terrestrial carbon cycle:  
 887 concepts, processes and potential future impacts. *Global change biology*, *21*(8),  
 888 2861–2880.
- 889 Friedl, M., & Sulla-Menashe, D. (2015). MCD12C1 MODIS/Terra+ Aqua Land  
 890 Cover Type Yearly L3 Global 0.05 Deg CMG V006 [Data set]. *NASA EOSDIS*  
 891 *Land Processes DAAC*.
- 892 Fu, D., Bowman, K. W., Worden, H. M., Natraj, V., Worden, J. R., Yu, S., ... Han,  
 893 Y. (2016). High-resolution tropospheric carbon monoxide profiles retrieved  
 894 from CrIS and TROPOMI. *Atmospheric Measurement Techniques*, *9*(6), 2567–  
 895 2579. Retrieved from <https://amt.copernicus.org/articles/9/2567/2016/>  
 896 doi: 10.5194/amt-9-2567-2016
- 897 Gelaro, R., McCarty, W., Suárez, M. J., Todling, R., Molod, A., Takacs, L., ...  
 898 others (2017). The modern-era retrospective analysis for research and applica-  
 899 tions, version 2 (MERRA-2). *J. Climate*, *30*(14), 5419–5454.
- 900 Giglio, L., Randerson, J. T., & Van Der Werf, G. R. (2013). Analysis of daily,  
 901 monthly, and annual burned area using the fourth-generation global fire emis-  
 902 sions database (gfed4). *Journal of Geophysical Research: Biogeosciences*,  
 903 *118*(1), 317–328.
- 904 Griffith, D. W., Velazco, V. A., Deutscher, N. M., Paton-Walsh, C., Jones, N. B.,  
 905 Wilson, S. R., ... Riggensbach, M. O. (2014). *TCCON data from Wollongong (AU), Release GGG2014.R0*. CaltechDATA. Retrieved from  
 906 <https://data.caltech.edu/records/291> doi: 10.14291/tcon.ggg2014  
 907 .wollongong01.r0/1149291
- 908
- 909 Guenther, A. B., Jiang, X., Heald, C. L., Sakulyanontvittaya, T., Duhl, T., Em-  
 910 mons, L. K., & Wang, X. (2012). The model of emissions of gases and aerosols  
 911 from nature version 2.1 (megan2.1): an extended and updated framework for  
 912 modeling biogenic emissions. *Geoscientific Model Development*, *5*(6), 1471–

- 913 1492. Retrieved from <https://gmd.copernicus.org/articles/5/1471/2012/>  
 914 doi: 10.5194/gmd-5-1471-2012
- 915 Guérette, E.-A., Paton-Walsh, C., Desservettaz, M., Smith, T. E. L., Volkova, L.,  
 916 Weston, C. J., & Meyer, C. P. (2018). Emissions of trace gases from Aus-  
 917 tralian temperate forest fires: emission factors and dependence on modified  
 918 combustion efficiency. *Atmospheric Chemistry and Physics*, *18*(5), 3717–3735.  
 919 Retrieved from <https://acp.copernicus.org/articles/18/3717/2018/>  
 920 doi: 10.5194/acp-18-3717-2018
- 921 Harris, S., & Lucas, C. (2019). Understanding the variability of Australian fire  
 922 weather between 1973 and 2017. *PloS one*, *14*(9), e0222328.
- 923 Haverd, V., Ahlström, A., Smith, B., & Canadell, J. G. (2017). Carbon cycle re-  
 924 sponses of semi-arid ecosystems to positive asymmetry in rainfall. *Global*  
 925 *change biology*, *23*(2), 793–800. doi: 10.1111/gcb.13412
- 926 He, L., Wood, J. D., Sun, Y., Magney, T., Dutta, D., Köhler, P., ... Frankenberg,  
 927 C. (2020). Tracking seasonal and interannual variability in photosynthetic  
 928 downregulation in response to water stress at a temperate deciduous forest.  
 929 *Journal of Geophysical Research: Biogeosciences*, *125*(8), e2018JG005002.
- 930 Henze, D. K., Hakami, A., & Seinfeld, J. H. (2007). Development of the adjoint of  
 931 GEOS-Chem. *Atmos. Chem. Phys.*, *7*(9), 2413–2433.
- 932 Herold, N., Downes, S., Gross, M., Ji, F., Nishant, N., Macadam, I., ... Beyer, K.  
 933 (2021). Projected changes in the frequency of climate extremes over southeast  
 934 Australia. *Environmental Research Communications*, *3*(1), 011001.
- 935 Hirsch, E., & Koren, I. (2021). Record-breaking aerosol levels explained by smoke in-  
 936 jection into the stratosphere. *Science*, *371*(6535), 1269–1274.
- 937 Huxman, T. E., Snyder, K. A., Tissue, D., Leffler, A. J., Ogle, K., Pockman, W. T.,  
 938 ... Schwinning, S. (2004). Precipitation pulses and carbon fluxes in semiarid  
 939 and arid ecosystems. *Oecologia*, *141*(2), 254–268.
- 940 Joiner, J., & Yoshida, Y. (2020). Satellite-based reflectances capture large fraction  
 941 of variability in global gross primary production (GPP) at weekly time scales.  
 942 *Agricultural and Forest Meteorology*, *291*, 108092.
- 943 Kaiser, J. W., Heil, A., Andreae, M. O., Benedetti, A., Chubarova, N., Jones, L.,  
 944 ... van der Werf, G. R. (2012). Biomass burning emissions estimated with  
 945 a global fire assimilation system based on observed fire radiative power. *Bio-*  
 946 *geosciences*, *9*(1), 527–554. Retrieved from [https://bg.copernicus.org/](https://bg.copernicus.org/articles/9/527/2012/)  
 947 [articles/9/527/2012/](https://bg.copernicus.org/articles/9/527/2012/) doi: 10.5194/bg-9-527-2012
- 948 Karna, Y. K., Penman, T. D., Aponte, C., & Bennett, L. T. (2019). Assessing legacy  
 949 effects of wildfires on the crown structure of fire-tolerant eucalypt trees using  
 950 airborne lidar data. *Remote Sensing*, *11*(20), 2433.
- 951 Khaykin, S., Legras, B., Bucci, S., Sellitto, P., Isaksen, L., Tence, F., ... others  
 952 (2020). The 2019/20 Australian wildfires generated a persistent smoke-charged  
 953 vortex rising up to 35 km altitude. *Communications Earth & Environment*,  
 954 *1*(1), 1–12.
- 955 King, A. D., Pitman, A. J., Henley, B. J., Ukkola, A. M., & Brown, J. R. (2020).  
 956 The role of climate variability in Australian drought. *Nature Climate Change*,  
 957 *10*(3), 177–179.
- 958 Kirono, D. G., Round, V., Heady, C., Chiew, F. H., & Osbrough, S. (2020). Drought  
 959 projections for Australia: updated results and analysis of model simulations.  
 960 *Weather and Climate Extremes*, *30*, 100280.
- 961 Kuhns, H., Green, M., Etyemezian, V., Watson, J., & Pitchford, M. (2003). Big  
 962 bend regional aerosol and visibility observational (BRAVO) study emissions  
 963 inventory. *Report prepared for BRAVO Steering Committee, Desert Research*  
 964 *Institute, Las Vegas, Nevada*.
- 965 Landgraf, J., aan de Brugh, J., Scheepmaker, R., Borsdorff, T., Hu, H., Houweling,  
 966 S., ... Hasekamp, O. (2016). Carbon monoxide total column retrievals from  
 967 TROPOMI shortwave infrared measurements. *Atmospheric Measurement Tech-*

- 968 *niques*, 9(10), 4955–4975. Retrieved from [https://amt.copernicus.org/](https://amt.copernicus.org/articles/9/4955/2016/)  
 969 [articles/9/4955/2016/](https://doi.org/10.5194/amt-9-4955-2016) doi: 10.5194/amt-9-4955-2016
- 970 Langenfelds, R., Francey, R., Pak, B., Steele, L., Lloyd, J., Trudinger, C., & Allison,  
 971 C. (2002). Interannual growth rate variations of atmospheric  $\text{CO}_2$  and its  $\delta^{13}\text{C}$ ,  
 972  $\text{H}_2$ ,  $\text{CH}_4$ , and  $\text{CO}$  between 1992 and 1999 linked to biomass burning. *Global*  
 973 *Biogeochemical Cycles*, 16(3), 21–1.
- 974 Li, L., Wang, Y.-P., Beringer, J., Shi, H., Cleverly, J., Cheng, L., ... others (2017).  
 975 Responses of LAI to rainfall explain contrasting sensitivities to carbon uptake  
 976 between forest and non-forest ecosystems in Australia. *Scientific reports*, 7(1),  
 977 1–9.
- 978 Lindenmayer, D., Blair, D., McBurney, L., Banks, S., & Bowd, E. (2021). Ten  
 979 years on—a decade of intensive biodiversity research after the 2009 black sat-  
 980 urday wildfires in Victoria’s mountain ash forest. *Australian Zoologist*, 41(2),  
 981 220–230.
- 982 Liu, J., Bowman, K. W., Lee, M., Henze, D. K., Bousserrez, N., Brix, H., ... others  
 983 (2014). Carbon monitoring system flux estimation and attribution: impact  
 984 of ACOS-GOSAT  $\text{XCO}_2$  sampling on the inference of terrestrial biospheric  
 985 sources and sinks. *Tellus B*, 66(1), 22486. doi: 10.3402/tellusb.v66.22486
- 986 Liu, J., Bowman, K. W., Schimel, D. S., Parazoo, N. C., Jiang, Z., Lee, M., ...  
 987 Eldering, A. (2017). Contrasting carbon cycle responses of the tropical  
 988 continents to the 2015–2016 El Niño. *Science*, 358(6360). Retrieved from  
 989 <http://science.sciencemag.org/content/358/6360/eam5690> doi:  
 990 10.1126/science.aam5690
- 991 Longo, M., Saatchi, S., Keller, M., Bowman, K. W., Ferraz, A., Moorcroft, P. R., ...  
 992 others (2020). Impacts of degradation on water, energy, and carbon cycling of  
 993 the Amazon tropical forests. *Journal of Geophysical Research: Biogeosciences*,  
 994 125(8), e2020JG005677.
- 995 Masarie, K., Peters, W., Jacobson, A., & Tans, P. (2014). Obspack: a framework  
 996 for the preparation, delivery, and attribution of atmospheric greenhouse gas  
 997 measurements. *Earth Syst. Sci. Data*, 6(2), 375–384.
- 998 Mu, M., Randerson, J., Van der Werf, G., Giglio, L., Kasibhatla, P., Morton, D.,  
 999 ... others (2011). Daily and 3-hourly variability in global fire emissions and  
 1000 consequences for atmospheric model predictions of carbon monoxide. *Journal*  
 1001 *of Geophysical Research: Atmospheres*, 116(D24).
- 1002 Muñoz Sabater, J. (2019). *Copernicus Climate Change Service (C3S) Climate Data*  
 1003 *Store (CDS)*. (2020-08-11) doi: 10.24381/cds.68d2bb30
- 1004 Nolan, R. H., Boer, M. M., Collins, L., Resco de Dios, V., Clarke, H., Jenkins, M.,  
 1005 ... Bradstock, R. A. (2020). Causes and consequences of eastern Australia’s  
 1006 2019–20 season of mega-fires. *Global change biology*, 26(3), 1039–1041.
- 1007 Nolan, R. H., Gauthey, A., Losso, A., Medlyn, B. E., Smith, R., Chhajer, S. S., ...  
 1008 others (2021). Hydraulic failure and tree size linked with canopy die-back in  
 1009 eucalypt forest during extreme drought. *New Phytologist*.
- 1010 Olivier, J., & Berdowski, J. (2001). Global emissions sources and sinks. the climate  
 1011 system. *Lisse, The Netherlands: AA Balkema Publishers/Swets & Zeitlinger*  
 1012 *Publishers*90, 5809(255), 0.
- 1013 Paton-Walsh, C., Smith, T., Young, E., Griffith, D. W., & Guérette, É.-A. (2014).  
 1014 New emission factors for Australian vegetation fires measured using open-path  
 1015 fourier transform infrared spectroscopy—part 1: Methods and Australian tem-  
 1016 perate forest fires. *Atmospheric Chemistry and Physics*, 14(20), 11313–11333.
- 1017 Pellegrini, A. F., Refsland, T., Averill, C., Terrer, C., Staver, A. C., Brockway,  
 1018 D. G., ... others (2021). Decadal changes in fire frequencies shift tree commu-  
 1019 nities and functional traits. *Nature Ecology & Evolution*, 5(4), 504–512.
- 1020 Perkins-Kirkpatrick, S., & Gibson, P. (2017). Changes in regional heatwave char-  
 1021 acteristics as a function of increasing global temperature. *Scientific Reports*,  
 1022 7(1), 1–12.

- 1023 Pitman, A., Narisma, G., & McAneney, J. (2007). The impact of climate change on  
1024 the risk of forest and grassland fires in australia. *Climatic Change*, *84*(3), 383–  
1025 401.
- 1026 Pollard, D. F., Robinson, J., & Shiona., H. (2019). *TCCON data from Lauder, New*  
1027 *Zealand, 125HR, release GGG2014R0*. CaltechDATA. doi: 10.14291/tcon  
1028 .ggg2014.lauder03.R0
- 1029 Pollard, D. F., Sherlock, V., Robinson, J., Deutscher, N. M., Connor, B., & Sh-  
1030 iona, H. (2017). The total carbon column observing network site description  
1031 for lauder new zealand. *Earth System Science Data*, *9*(2), 977–992. Re-  
1032 trieved from <https://essd.copernicus.org/articles/9/977/2017/> doi:  
1033 10.5194/essd-9-977-2017
- 1034 Poulter, B., Frank, D., Ciais, P., Myneni, R. B., Andela, N., Bi, J., . . . others  
1035 (2014). Contribution of semi-arid ecosystems to interannual variability of  
1036 the global carbon cycle. *Nature*, *509*(7502), 600.
- 1037 Randerson, J. T., Chen, Y., Van Der Werf, G., Rogers, B., & Morton, D. (2012).  
1038 Global burned area and biomass burning emissions from small fires. *Journal of*  
1039 *Geophysical Research: Biogeosciences*, *117*(G4).
- 1040 Reichstein, M., Ciais, P., Papale, D., Valentini, R., Running, S., Viovy, N., . . . oth-  
1041 ers (2007). Reduction of ecosystem productivity and respiration during the  
1042 european summer 2003 climate anomaly: a joint flux tower, remote sensing  
1043 and modelling analysis. *Global Change Biology*, *13*(3), 634–651.
- 1044 Rémy, S., Veira, A., Paugam, R., Sofiev, M., Kaiser, J. W., Marenco, F., . . . Hair,  
1045 J. W. (2017). Two global data sets of daily fire emission injection heights  
1046 since 2003. *Atmospheric Chemistry and Physics*, *17*(4), 2921–2942. Re-  
1047 trieved from <https://acp.copernicus.org/articles/17/2921/2017/> doi:  
1048 10.5194/acp-17-2921-2017
- 1049 Schaaf, C. B., Gao, F., Strahler, A. H., Lucht, W., Li, X., Tsang, T., . . . others  
1050 (2002). First operational BRDF, albedo nadir reflectance products from  
1051 MODIS. *Remote sensing of Environment*, *83*(1-2), 135–148.
- 1052 Schwartz, M. J., Santee, M. L., Pumphrey, H. C., Manney, G. L., Lambert, A.,  
1053 Livesey, N. J., . . . Werner, F. (2020). Australian New Year’s PyroCb im-  
1054 pact on stratospheric composition. *Geophysical Research Letters*, *47*(24),  
1055 e2020GL090831.
- 1056 Sharples, J. J., Cary, G. J., Fox-Hughes, P., Mooney, S., Evans, J. P., Fletcher, M.-  
1057 S., . . . Baker, P. (2016). Natural hazards in Australia: extreme bushfire.  
1058 *Climatic Change*, *139*(1), 85–99.
- 1059 Shiraishi, T., & Hirata, R. (2021). Estimation of carbon dioxide emissions from the  
1060 megafires of Australia in 2019–2020. *Scientific reports*, *11*(1), 1–10.
- 1061 Silva, L. G., Doyle, K. E., Duffy, D., Humphries, P., Horta, A., & Baumgartner,  
1062 L. J. (2020). Mortality events resulting from Australia’s catastrophic fires  
1063 threaten aquatic biota. *Global Change Biology*, *26*(10), 5345–5350.
- 1064 Sippel, S., Reichstein, M., Ma, X., Mahecha, M. D., Lange, H., Flach, M., & Frank,  
1065 D. (2018). Drought, heat, and the carbon cycle: a review. *Current Climate*  
1066 *Change Reports*, 1–21.
- 1067 Stanevich, I., Jones, D. B. A., Strong, K., Keller, M., Henze, D. K., Parker, R. J., . . .  
1068 Deng, F. (2019). Characterizing model errors in chemical transport modelling  
1069 of methane: Using GOSAT X<sub>CH<sub>4</sub></sub> data with weak constraint four-dimensional  
1070 variational data assimilation. *Atmospheric Chemistry and Physics Discus-*  
1071 *sions*, *2019*, 1–54. Retrieved from [https://acp.copernicus.org/preprints/](https://acp.copernicus.org/preprints/acp-2019-786/)  
1072 [acp-2019-786/](https://acp-2019-786/) doi: 10.5194/acp-2019-786
- 1073 Stephens, S. L., Agee, J. K., Fule, P. Z., North, M., Romme, W., Swetnam, T., &  
1074 Turner, M. G. (2013). Managing forests and fire in changing climates. *Science*,  
1075 *342*(6154), 41–42.
- 1076 Streets, D. G., Zhang, Q., Wang, L., He, K., Hao, J., Wu, Y., . . . Carmichael, G. R.  
1077 (2006). Revisiting China’s CO emissions after the transport and chemical

- 1078 evolution over the pacific (TRACE-P) mission: Synthesis of inventories, at-  
 1079 mospheric modeling, and observations. *Journal of Geophysical Research:*  
 1080 *Atmospheres*, 111(D14).
- 1081 Sun, Q., Meyer, W. S., Koerber, G. R., & Marschner, P. (2020). Rapid recovery of  
 1082 net ecosystem production in a semi-arid woodland after a wildfire. *Agricultural*  
 1083 *and Forest Meteorology*, 291, 108099.
- 1084 Sun, Y., Fu, R., Dickinson, R., Joiner, J., Frankenberg, C., Gu, L., ... Fernando, N.  
 1085 (2015). Drought onset mechanisms revealed by satellite solar-induced chloro-  
 1086 phyll fluorescence: Insights from two contrasting extreme events. *Journal of*  
 1087 *Geophysical Research: Biogeosciences*, 120(11), 2427–2440.
- 1088 Turner, A. J., Köhler, P., Magney, T. S., Frankenberg, C., Fung, I., & Cohen,  
 1089 R. C. (2020). A double peak in the seasonality of california’s photo-  
 1090 synthesis as observed from space. *Biogeosciences*, 17(2), 405–422. Re-  
 1091 trieved from <https://bg.copernicus.org/articles/17/405/2020/> doi:  
 1092 10.5194/bg-17-405-2020
- 1093 Ukkola, A. M., De Kauwe, M. G., Roderick, M. L., Abramowitz, G., & Pitman,  
 1094 A. J. (2020). Robust future changes in meteorological drought in CMIP6  
 1095 projections despite uncertainty in precipitation. *Geophysical Research Letters*,  
 1096 47(11), e2020GL087820.
- 1097 van der Werf, G. R., Randerson, J. T., Giglio, L., van Leeuwen, T. T., Chen,  
 1098 Y., Rogers, B. M., ... Kasibhatla, P. S. (2017). Global fire emissions  
 1099 estimates during 1997–2016. *Earth Syst. Sci. Data*, 9(2), 697–720. Re-  
 1100 trieved from <https://www.earth-syst-sci-data.net/9/697/2017/> doi:  
 1101 10.5194/essd-9-697-2017
- 1102 Veefkind, J., Aben, I., McMullan, K., Förster, H., De Vries, J., Otter, G., ... others  
 1103 (2012). TROPOMI on the ESA Sentinel-5 Precursor: A GMES mission for  
 1104 global observations of the atmospheric composition for climate, air quality and  
 1105 ozone layer applications. *Remote sensing of environment*, 120, 70–83.
- 1106 Vestreng, V. (2002). Emission data reported to UNECE/EMEP: Quality assurance  
 1107 and trend analysis & presentation of WebDab: MSC-W status report 2002.
- 1108 Volkova, L., Aparicio, A. G. W., & Weston, C. J. (2019). Fire intensity effects on  
 1109 post-fire fuel recovery in eucalyptus open forests of south-eastern Australia.  
 1110 *Science of the total environment*, 670, 328–336.
- 1111 Wang, C., Corbett, J. J., & Firestone, J. (2008). Improving spatial representation of  
 1112 global ship emissions inventories. *Environmental Science & Technology*, 42(1),  
 1113 193–199.
- 1114 Wang, J., Liu, Z., Zeng, N., Jiang, F., Wang, H., & Ju, W. (2020). Spaceborne de-  
 1115 tection of X<sub>CO<sub>2</sub></sub> enhancement induced by Australian mega-bushfires. *Environ-*  
 1116 *mental Research Letters*, 15(12), 124069.
- 1117 Wang, J., Wang, M., Kim, J.-S., Joiner, J., Zeng, N., Jiang, F., ... others (2021).  
 1118 Modulation of land photosynthesis by the indian ocean dipole: Satellite-  
 1119 based observations and CMIP6 future projections. *Earth’s Future*, 9(4),  
 1120 e2020EF001942.
- 1121 Ward, M., Tulloch, A. I., Radford, J. Q., Williams, B. A., Reside, A. E., Macdonald,  
 1122 S. L., ... others (2020). Impact of 2019–2020 mega-fires on Australian fauna  
 1123 habitat. *Nature Ecology & Evolution*, 4(10), 1321–1326.
- 1124 Waring, R., Landsberg, J., & Williams, M. (1998). Net primary production of  
 1125 forests: a constant fraction of gross primary production? *Tree physiology*,  
 1126 18(2), 129–134.
- 1127 Wunch, D., Toon, G. C., Blavier, J.-F. L., Washenfelder, R. A., Notholt, J., Con-  
 1128 nor, B. J., ... Wennberg, P. O. (2011). The Total Carbon Column Ob-  
 1129 serving Network. *Philos. T. Roy. Soc. A*, 369(1943), 2087–2112. doi:  
 1130 10.1098/rsta.2010.0240
- 1131 Yin, Y., Bloom, A. A., Worden, J., Saatchi, S., Yang, Y., Williams, M., ... Schimel,  
 1132 D. (2020). Fire decline in dry tropical ecosystems enhances decadal land car-

- 1133 bon sink. *Nature Communications*, 11(1), 1900. Retrieved from [https://](https://doi.org/10.1038/s41467-020-15852-2)  
 1134 [doi.org/10.1038/s41467-020-15852-2](https://doi.org/10.1038/s41467-020-15852-2) doi: 10.1038/s41467-020-15852-2
- 1135 Yin, Y., Byrne, B., Liu, J., Wennberg, P. O., Davis, K. J., Magney, T., ... others  
 1136 (2020). Cropland carbon uptake delayed and reduced by 2019 midwest floods.  
 1137 *AGU Advances*, 1(1), e2019AV000140.
- 1138 Yin, Y., Chevallier, F., Ciais, P., Broquet, G., Fortems-Cheiney, A., Pison, I.,  
 1139 & Saunois, M. (2015, dec). Decadal trends in global CO emissions as  
 1140 seen by MOPITT. *Atmospheric Chemistry and Physics*, 15(23), 13433–  
 1141 13451. Retrieved from [http://www.atmos-chem-phys.net/15/13433/2015/](http://www.atmos-chem-phys.net/15/13433/2015/acp-15-13433-2015.html)  
 1142 [acp-15-13433-2015.html](http://www.atmos-chem-phys.net/15/13433-2015.html) doi: 10.5194/acp-15-13433-2015
- 1143 Yin, Y., Ciais, P., Chevallier, F., van der Werf, G. R., Fanin, T., Broquet, G.,  
 1144 ... Wang, Y. (2016). Variability of fire carbon emissions in Equatorial  
 1145 Asia and its non-linear sensitivity to El Niño. *Geophysical Research Let-*  
 1146 *ters*. Retrieved from <http://doi.wiley.com/10.1002/2016GL070971> doi:  
 1147 10.1002/2016GL070971
- 1148 Yoshida, Y., Joiner, J., Tucker, C., Berry, J., Lee, J.-E., Walker, G., ... Wang, Y.  
 1149 (2015). The 2010 Russian drought impact on satellite measurements of solar-  
 1150 induced chlorophyll fluorescence: Insights from modeling and comparisons with  
 1151 parameters derived from satellite reflectances. *Remote Sensing of Environ-*  
 1152 *ment*, 166, 163–177.
- 1153 Zhang, Y., Xiao, X., Zhou, S., Ciais, P., McCarthy, H., & Luo, Y. (2016). Canopy  
 1154 and physiological controls of GPP during drought and heat wave. *Geophysical*  
 1155 *Research Letters*, 43(7), 3325–3333.
- 1156 Zheng, B., Chevallier, F., Yin, Y., Ciais, P., Fortems-Cheiney, A., Deeter, M. N., ...  
 1157 Zhao, Y. (2019, sep). Global atmospheric carbon monoxide budget 2000–2017  
 1158 inferred from multi-species atmospheric inversions. *Earth System Science Data*,  
 1159 11(3), 1411–1436. Retrieved from [https://www.earth-syst-sci-data.net/](https://www.earth-syst-sci-data.net/11/1411/2019/)  
 1160 11/1411/2019/ doi: 10.5194/essd-11-1411-2019